Supplementary Online Materials (SOM-S1): Survey and Analytical Methods and Results

ERICH C. FISHER
Institute of Human Origins, School of Human Evolution and Social Change, Arizona State University, Tempe, AZ 85287-2402, USA; erich.fisher@asu.edu

ROSA-MARIA ALBERT
Institució Catalana de Recherca i Estudis Avançats (ICREA)/GEPEG—Research Group for Paleoecological and Geoarchaeological Studies, Department of Prehistory, Ancient History, and Archaeology, University of Barcelona, Montalegre, 6–8, Barcelona 08001, SPAIN; rmalbert@ub.edu

GREG BOTHA
Council for Geoscience, KwaZulu-Natal and Eastern Cape Units, 139 Jabu Ndlovu Street, Pietermaritzburg 3200, SOUTH AFRICA; gabotha@geoscience.org.za

HAYLEY C. CAWTHRA
Council for Geoscience, Marine Geoscience Unit, 3 Oos Street, Bellville, Capetown 7535, SOUTH AFRICA; hcawthra@geoscience.org.za

IRENE ESTEBAN
GEPEG—Research Group for Paleoecological and Geoarchaeological Studies, Department of Prehistory, Ancient History, and Archaeology, University of Barcelona, Montalegre, 6–8, Barcelona 08001, SPAIN; irene.esteban.alama@gmail.com

JACOB HARRIS
Institute of Human Origins, School of Human Evolution and Social Change, Arizona State University, Tempe, AZ 85287-2402, USA; Jacob.A.Harris@asu.edu

ZENOBIA JACOBS
Centre for Archaeological Science, School of Earth and Environmental Sciences, University of Wollongong, Northfields Avenue, Wollongong, New South Wales, 2522, AUSTRALIA; zenobia@uow.edu.au

ANTONIETA JERARDINO
ICREA/Department of Archaeology and Anthropology, CaSEs Research Group, Spanish National Research Council (CSIC-IMF), C/ de les Eguipcíaques 15, Barcelona 08001, SPAIN; a.jerardino@imf.csic.es

CURTIS W. MAREAN
Institute of Human Origins, School of Human Evolution and Social Change, Arizona State University, Tempe, AZ 85287-2402, USA; curtis.marean@asu.edu

FRANK H. NEUMANN
Forschungsstelle Paläobotanik, Westfälische Wilhelms-Universität Münster, Heisenbergstrasse 2, 48149 Münster, GERMANY; fneumann1971@googlemail.com

JUSTIN PARGETER
Department of Anthropology, SUNY-Stony Brook University, Circle Road, Stony Brook, NY 11794, USA; justin.pargeter@stonybrook.edu

MELANIE POUPART
Department of Anthropology, McGill University, 855 Sherbrooke Street West, Leacock Building, Room 718, Montreal, Quebec H3A 2T7, CANADA; melanie.poupart@mail.mcgill.ca

JAN VENTER
Centre for Wildlife Management, University of Pretoria, Private Bag X20, Hatfield, Pretoria 0028, SOUTH AFRICA; Jan.Venter@ecpta.co.za

***PaleoAnthropology* 2013: S1–27.** **© 2013 PaleoAnthropology Society. All rights reserved.** **ISSN 1545-0031**
doi:10.4207/PA.2013.ART82.dat1

SURVEY METHODOLOGY

The survey was conducted on foot. It was limited to within 5km of the coastline, which guaranteed that any sites we found would have almost certainly been within a presumed 10km hunter-gatherer coastal foraging distance during the Pleistocene. The survey area was gridded into 10km^2 blocks based on the UTM coordinate system (WGS84 datum, zones 35s and 36s). Each grid block was labeled alphanumerically as shown in Supplementary Online Materials, Section 1, Figure 1 **(**Figure 1**)**. These blocks were further subdivided into 5km^2 quadrants (NW, NE, SE, SW). Site names used the convention: *Gridblock, Quadrant, -numerical count of the site within the quadrant*. For example, site C4NW-2 was the second site found in the NW quadrant of block C4. The survey proceeded through grid blocks systematically, targeting riverine valleys first, coastal zones second, grasslands, and then forests.

The grid and grid blocks were organized into a key map booklet that included general reference information on the surficial geology as well as 1:70,000 scale individual pages for each alphanumeric grid zone (see Figure 1; Figure 2**)**. The booklet was spiral bound so that it could be folded over. It was also printed on card stock to make the pages sturdy and it was professionally laminated for water proofing. The lamination even allowed field team members to annotate onto the pages directly using a permanent marker, which could still be "erased" with rubbing alcohol (Figure 3**)**. The end of the map booklet included an artifact photograph page that had a 1 cm grid (with mm annotations) and 50% grey, 18% grey, black, and white color targets to adjust for color cast and contrast in digital image post-processing **(**Figure 4**).** There was also a lineated page with a scale that was frequently used to annotate field photographs **(**Figure 5**)**.

During the survey, the four-person field team divided into pairs to cover larger areas more effectively. Both teams kept GPS logs of their progress. Upon finding an area of interest, a radio call brought the team together to record the site. We used standardized field forms to record basic location, contextual, and descriptive information about each site. These data were supplemented by abundant personal notes and drawings of visible artifacts, faunal remains, and geology. Each site or sample location was also preliminarily mapped and the surficial artifacts and faunal remains were cataloged, but no archaeological or faunal materials were collected or removed from the sites. We also collected extensive photography, and some video, using a Nikon D300s camera. We used a Nikon GP-1 to automatically geotag photographs in areas with good sky visibility. Field forms were entered into an Access database nightly and copies of the forms as well as of the field books were also digitized. All photography and GPS logs were similarly backed up onto a laptop.

SEDIMENT CORING

Sediment core locations were chosen to sample across our study area from south to north. We sought locations where there were multiple vegetation zones present. We used a 3"

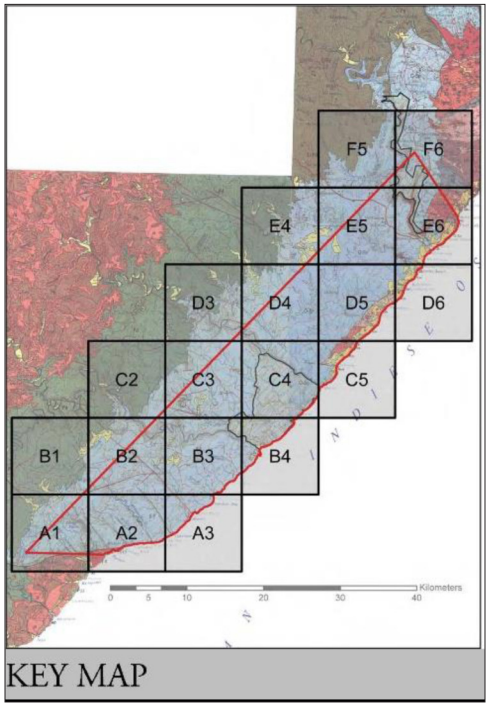

Figure 1. Key map of the P5 2011 survey showing the survey area and alphanumeric grid overlaying a geological base map. Each grid square corresponds to a separate page in the booklet.

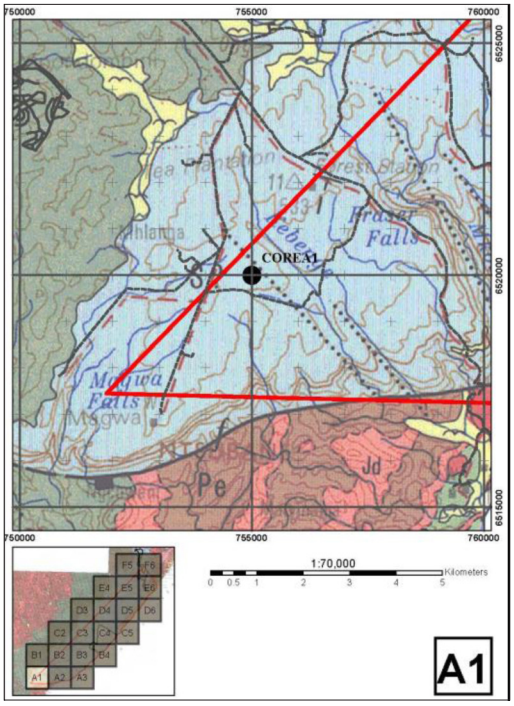

Figure 2. Grid pages from survey booklet. The main map box is shown at 1:70K scale. The area is subdivided into 5km^2 quads, and includes roads, rivers, and populated places. Potential sediment core locations were also shown. The grid is highlighted in the mini-key map in the lower left.

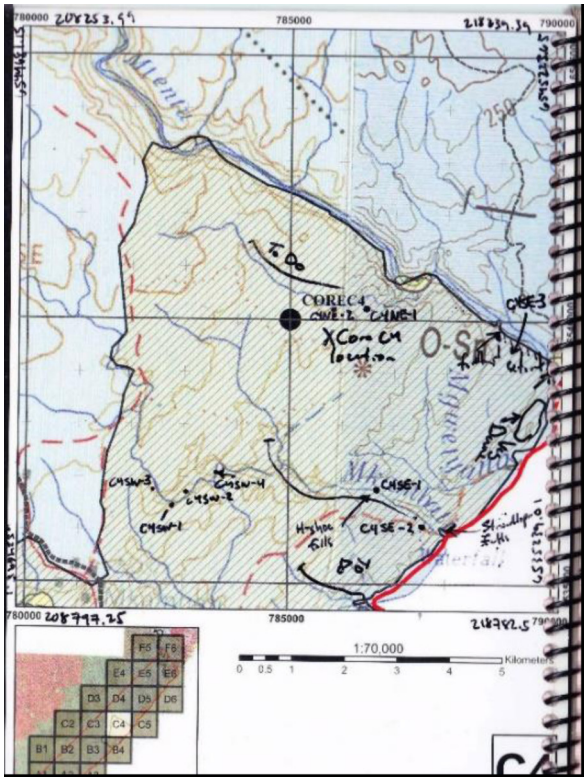

Figure 3. Annotation on grid page C4 from the field book of ECF. The annotation denotes task to complete, site locations, and assorted notes useful during the survey.

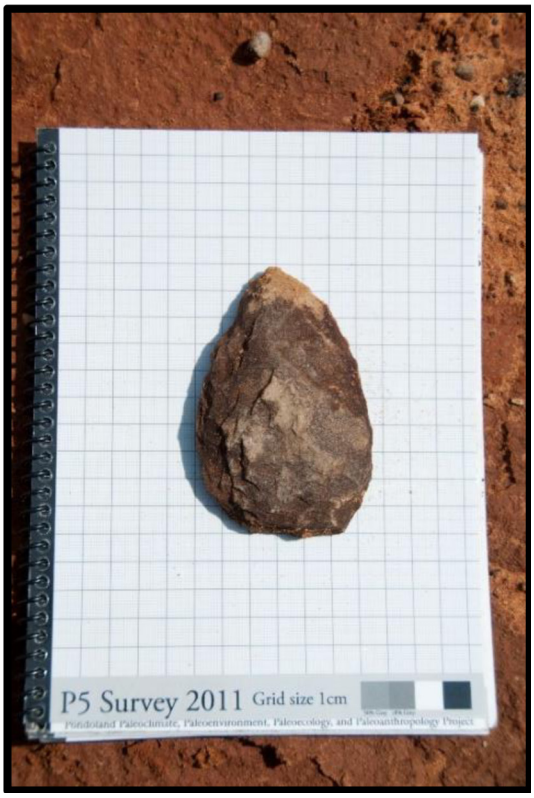

Figure 4. The artifact photograph page showing an artifact from B4NW-1 on the 1cm grid. The color cast targets are visible in the lower right corner.

Figure 5. The lineated page at the back of the map booklet was useful for annotating photographs. A 10cm scale was also included for reference on the page. Note the spiral design that allowed the pages to be folded over.

Figure 6. HC starting to core C4 with JP assisting and MP recording samples.

diameter augur to collect **3** vertical transects of sediment within our study area. The samples were collected every 20cm (Figure 6**)**. Each sample was subdivided into smaller bags for pollen, phytoliths, and sediment geochemistry.

Of the three cores collected, two were selected for detailed analysis (B4-2 and C4). Core B3 was omitted from the current study because it was located peripheral to our main research area. We intend to study this core in the future, however. The basic sedimentology of cores B4-2 and C4 are provided in Figures 7 and 8. Table 1 provides additional descriptions of the sedimentology per sample.

TABLE 1. DETAILS ABOUT EACH CORE SAMPLE.*

Sample Number	Core	Depth, cm	Color	Sediment
12	C4	0–20	Brownish black	Clayey silt
13	C4	20–40	Brownish black	Clayey silt
14	C4	40–60	Olive black	Clayey silt
15	C4	60–80	Olive black	Clayey silt
16	C4	80–100	Dusky brown	Clayey silt
17	C4	100–120	Dusky yellowish brown	Clayey silt
18	C4	120–140	Dusky yellowish brown	Sandy clay
19	C4	140–160	Greyish brown	Sandy clay
20	C4	160–180	Dark yellowish brown	Clayey gravel
21	C4	180–200	Dark yellowish brown	Clayey gravel
22	C4	200–220	Moderate yellowish brown	Clayey gravel
23	C4	220–240	Moderate yellowish brown	Clayey sand
24	C4	240–260	Pale yellowish brown	Clayey sand
25	C4	260–280	Greyish orange	Clayey sand
26	C4	280–300	Greyish orange	Sand
27	C4	300–320	Greyish orange	Sand
28	C4	320–340	Greyish orange	Sand

TABLE 1. DETAILS ABOUT EACH CORE SAMPLE (continued).*

Sample Number	Core	Depth, cm	Color	Sediment
53	B4-2	0–20	Moderate reddish brown	Silty sand
54	B4-2	20–40	Moderate reddish brown	Silty sand
55	B4-2	40–60	Moderate reddish brown	Silty sand
56	B4-2	60–80	Moderate brown	Silty sand
57	B4-2	80–100	Moderate brown	Silty sand
58	B4-2	100–120	Moderate brown	Silty sand
59	B4-2	120–140	Moderate brown	Silty sand
60	B4-2	140–160	Moderate brown	Silty sand
61	B4-2	160–180	Moderate brown	Silty sand
62	B4-2	180–200	Moderate brown	Silty sand
63	B4-2	200–220	Moderate brown	Silty sand
64	B4-2	220–240	Moderate brown	Silty sand
65	B4-2	240–260	Moderate brown	Fine sand
66	B4-2	260–280	Moderate brown	Fine sand
67	B4-2	280–300	Moderate brown	Silty sand
68	B4-2	300–320	Moderate brown	Clayey silt
69	B4-2	320–340	Dark reddish brown	Clayey silt
70	B4-2	340–360	Dark reddish brown	Clayey sand
71	B4-2	360–380	Dark reddish brown	Clayey sand
72	B4-2	380–400	Dark reddish brown	Clayey silt
73	B4-2	400–420	Dark reddish brown	Clayey silt
74	B4-2	420–440	Dark reddish brown	Clayey silt
75	B4-2	440–460	Dark reddish brown	Clayey silt
76	B4-2	460–480	Dark reddish brown	Clayey silt
77	B4-2	480–-500	Dark reddish brown	Clayey silt
78	B4-2	500–520	Moderate reddish brown	Silty clay
79	B4-2	520–540	Moderate reddish brown	Silty clay
80	B4-2	540–560	Greyish red	Silty clay

*Samples used for the pollen and phytolith analysis described in the text were taken from core C4, Samples 12–28.

SEDIMENT CORE SAMPLES

All samples recovered from core C4 and B4 are listed in-Table 1. Preliminary descriptive data are also included.

PHYTOLITH ANALYSIS

The phytolith extraction was carried out at the Laboratory of Prehistory, Ancient History and Archaeology at the University of Barcelona using the rapid phytolith extraction procedure. Details of this method are described in Katz et al. (2010).

Methods

Between 30mg and 50mg of the sediment was placed into a 0.5ml Eppendorf plastic centrifuge tube. Carbonate minerals and carbonated hydroxylapatite were dissolved in 50 microliters of 6 N HCl using a micropipette (Finnpipette). 450ml 2.4g/ml sodium polytungstate solution [$Na_6(H_2W_{12}O_{40})vH_2O$] was then added after the bubbling had ceased. The tube was vortexed and sonicated for ~10 min (Ultrasons, Selecta), vortexed again, and then centrifuged finally for 5 min at 5000rpm (MiniSpin plus, Ep-

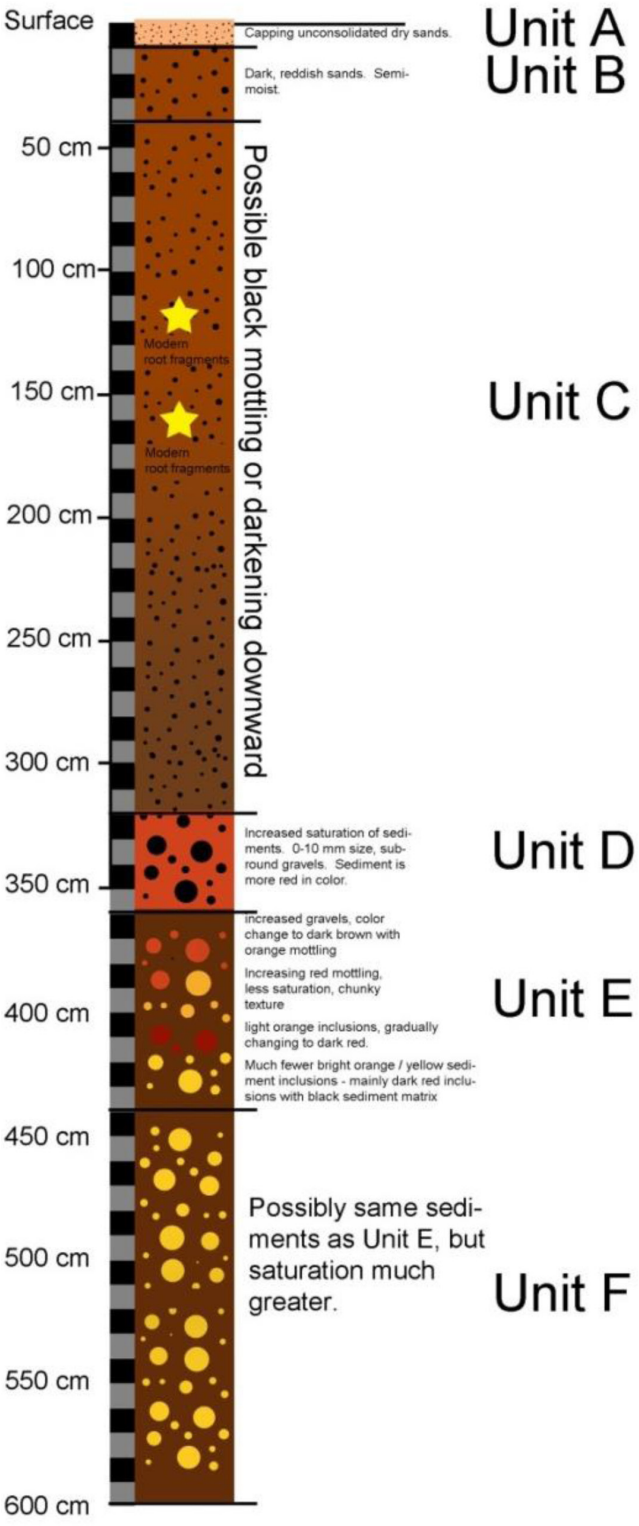

Figure 7. Core B4-2 was located at N 6528353, E 771828 (UTM Zone 35S) within a marsh on the inland edge of the rubified paleosol where site B4NW-1 was located. We collected 28 sediment samples up to a depth of 5.6 meters below surface.

The core sediments were predominantly clayey at the bottom and sandy at the top. The clay content in the upper 3.00 meters of the core range from 0–5%, increasing to between 35–55% at the base. Gravels also increased in frequency with depth.

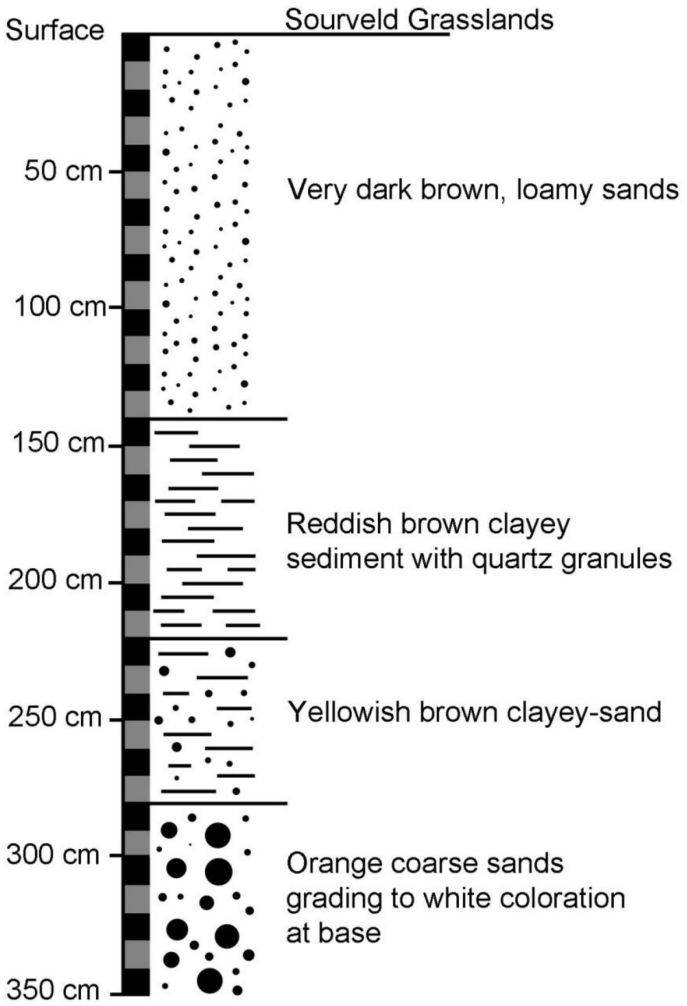

Figure 8. Core C4 was located at N 6539764 N, E 214670 (UTM Zone 36S) in the northern part of the Mkambati Game Reserve 2.5km from sites C4NE-1 and C4NE-2. The core was located in a grassland pasture adjacent to a shallow drainage, but it was within 0.5km of the Mtentu scarp forest. We collected 17 sediment samples up to a maximum depth of 3.4 meters below surface.

The core sediments ranged from sandy at the base to an intermediate clayey gravel (1.40–2.60 meters below surface). The uppermost sediments within 1.4 meters of the surface were clayey silts with ~5% clay fraction. The clay fraction was greater in the uppermost 40cm of sediments.

pendorf). The supernatant (phytoliths and charred organic material) was removed to a new 0.5ml centrifuge tube and vortexed one final time. Immediately after vortexing, a 50ml aliquot of the supernatant was placed on a microscope slide and covered with a 24mm x 24mm cover-slip. This slide was then examined under the optical microscope.

A general phytolith survey was conducted on 20 fields at 200x magnification. However, the morphological analysis relied on the identification of 200 phytoliths at 400x magnification in order to identify detailed morphological

TABLE 2. DESCRIPTON OF SAMPLES ANALYZED FROM CORE C4 AND ATTRIBUTES OF EACH SAMPLE RELEVANT TO THE PHYTOLITH ANALYSIS.

Sample	Depth (cm)	Sediment	Phytolith 1g/sed	% Diatoms	% Dissolution	FTIR
12	0–20	Very dark brown	3,000,000.00	0	7.56	Cl, Q
13	20–40	Very dark brown	3,000,000.00	0.52	6.76	Cl, Q
14	40–60	Very dark brown	3,500,000.00	0.57	7.45	Cl, Q
15	60–80	Very dark brown	2,500,000.00	0	7.18	Cl, Q
16	80–100	Very dark brown	2,400,000.00	1.23	10.06	Cl, Q
17	100–120	Very dark brown	2,300,000.00	1.5	7.94	Cl, Q
18	120–140	Very dark brown	1,000,000.00	2.52	21.09	Cl, Q
19	140–160	Reddish brown clayey	600,000.00	1.57	20.89	Cl, Q
20	160–180	Reddish brown clayey	500,000.00	0	25	Cl, Q
21	180–200	Reddish brown clayey	350,000.00	0	14.89	Cl, Q
22	200–220	Reddish brown clayey	200,000.00	0	25.86	Cl, Q
23	220–240	Yellowish brown clayey-sand	25,000.00			Cl, Q
24	240–260	Yellowish brown clayey-sand	10,000.00			Cl, Q
25	260–280	Yellowish brown clayey-sand	10,000.00			Cl, Q
26	280–300	Orange coarse sands	10,000.00			Cl, Q
27	300–320	Orange coarse sands	40,000.00			Cl, Q
28	320–330	Orange coarse sands	40,000.00			Cl, Q

characteristics of the phytoliths. The phytolith morphotypes were identified following our catalogue database (Albert et al. 2011) as well as standard literature (Mercader et al. 2000; Piperno 2006; Runge 1999; Twiss et al. 1969). Phytoliths are classified according to the anatomical origin of the plant in which they were from. When this is not possible, geometrical criteria are followed (Albert and Weiner 2001). The terminology used to describe the phytoliths follows, wherever possible, the International Code for Phytolith Nomenclature (ICPN) (Madella et al. 2005).

FTIR ANALYSIS

Infrared spectroscopy was used to identify the mineral components of the sediment. Infrared spectra were obtained using KBr pellets at 4cm^{-1} resolution with a Nicolet iS5 spectrometer. Variations in clay and quartz minerals were identified in the sediments by estimating their ratios using a quartz index described by Namdar et al. (2011). The height of the main silicate clay peak (1035cm^{-1}) was divided by the height of the silicate doublet (797cm^{-1}) to obtain the approximate quartz concentrations.

ANALYSIS OF CORE C4

Seventeen samples were analyzed for phytoliths from Core C4. Table 2 lists the provenance of each sample as well as the estimated number of phytoliths per gram of sediment, the percentage of phytoliths with dissolution traits, and FTIR results. Phytoliths were identified in all the samples. Diatoms and sponge spicules were also observed (Table 3; Figure 9G).

Phytolith Preservation

Phytolith and organic matter concentrations decreased with depth. Samples 12, 13 and 14, which were taken from the uppermost levels of the core, had the highest amount of phytoliths. Phytolith concentrations from these levels ranged from 3.5 to 3 million phytoliths per 1g of sediment. In contrast, samples from the lowermost levels only had 40,000 to 10,000 phytoliths per 1g of sediment. Similar reductions in phytolith and organic carbon concentrations have been observed in a number of other studies, showing that the rapidity of plant production cycles is largely responsible for the highest presence of phytoliths at the top

TABLE 3. PHYTOLITH MORPHOLOGICAL RESULTS FROM CORE C4.

	Sample Number										
Phytolith morphology	**12**	**13**	**14**	**15**	**16**	**17**	**18**	**19**	**20**	**21**	**22**
Bulliform	23.2	21.8	31.6	16.3	18.3	14.6	20.1	12.5	15	18.1	15.69
Brachiform		1.4									
Cylindroid psilate	2.8	5.9	4	1.5	1.7	4.3	2.9	1.3		2.3	2
Cylindroid rugulate	11	8.2	3	6.6	6.9	7.1	2.2	9.9	8.8	11.4	5.9
Cylindroid sinuous						1.4		0.7			
Cylindroid laminate		0.5	1	0.5		0.5		0.7			
Cylindroid bulbous							0.7				
Cylindroid diagonal lines					0.6						
Ellipsoid rugulate				1	1.1			0.7			2
Epidermal appendage Hair	1.1			1.5		0.9					
Epidermal appendage prickle	20.4	7.7	8.5	10.2	6.9	8.1	12.9	13.2	11.3	4.5	13.7
Long cell echinate	1.1	1.8	4.0	3.6	4.6	0.9		0.7			2.0
Long cell polylobate		0.9		1.0	0.6						
Parallelepiped blocky rugulate				1.0							
Parallelepiped elongate psilate		0.5	0.5	0.5	0.6	2.8		0.7			
Parallelepiped elongate rugulate	26.0	21.8	23.6	24.5	32.8	34.1	36.0	41.4	43.8	36.4	27.5
Parallelepiped thin psilate				0.5			1.4				
Parallelepiped thin rugulate	1.1	6.4	3.5	6.1	8.6	8.5	9.4	4.6	3.8	0.0	5.9
Parallelepiped facetate		2.3				0.9	0.7	2.0	2.5	2.3	2.0
Parallelepiped echinate	0.6	0.5	2.0	0.5	0.6					2.3	
Parallelepiped spiny	0.6	0.9	0.5	1.0	0.6		0.7	0.7			
Parallelepiped echinate one side		0.5	0.5	0.5	0.6						
Platelets				1.5		0.9					
Short cell rondel	2.2	3.2	3.0	4.6	1.1	3.3	1.4	0.7	1.3	2.3	2.0
Short cell bilobate	9.4	10.0	9.0	6.6	4.0	4.3	0.7	2.6	7.5	2.3	7.8
Short cell saddle		1.4	0.5	1.5	1.1	0.5					
Short cell cross shape		0.5			0.6	0.5					
Short cell tower											2.0
Trapeziform		0.9	0.5	2.0	0.6	1.9	1.4	2.6		11.4	3.9
Trapeziform sinuous										2.3	
Spheroid psilate		1.4	2.0		0.6						
Spheroid rugulate				0.5	1.1	0.9	3.6	0.7	1.3		2.0
Irregular psilate			1.5	4.1	4.0	2.8	2.9	2.6	5.0	4.5	5.9
Irregular rugulate							1.4				
Irregular echinate				0.5							
Indetermined	0.6	1.4	0.5	1.5	2.3	0.5	1.4	2.0			
Weathered morphotypes	6.7	6.0	6.6	6.7	9.4	7.5	18.3	17.8	21.6	13.7	22.7
Diatoms		0.5	0.5		1.1	1.4	2.1	1.3			
Sponge spicules	0.5										

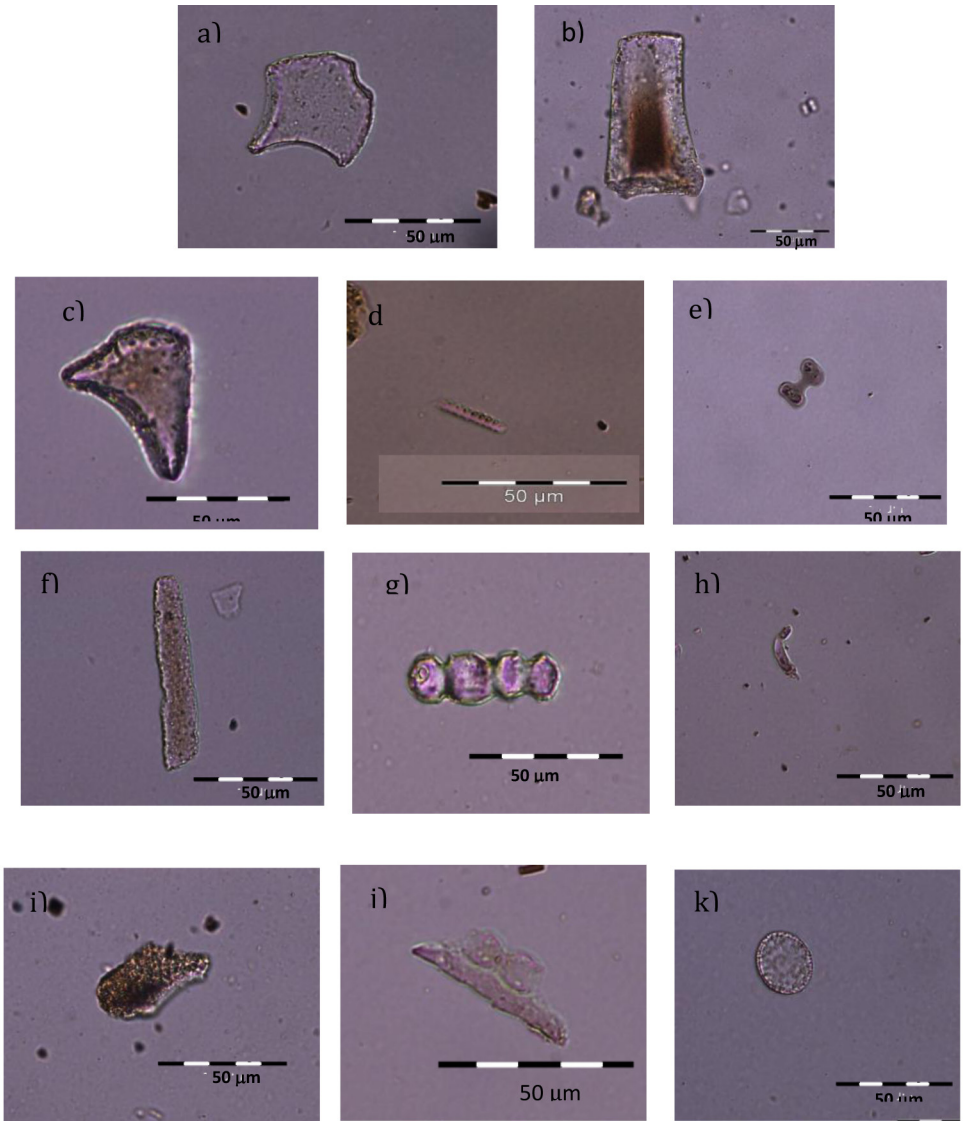

Figure 9. Microphotographs of phytoliths identified in samples from the Core C4: (a) Bullifom Fan-shape from sample 19; (b) Bulliform parallelepiped from sample 14; (c) Eppidermal appendage prickle from sample 20; (d) Long cell echinate from sample 16; (e) Short cell bilobate from sample 19; (f) Parallelepiped elongate rugulate from sample 20; (g) Multicellular spheroid rugulate from sample 18; (h) Eppidermal appendage hair from sample 15; (i) Weathered morphotype from sample 17; (j) Multicellular long cell and short cell bilobate from sample 12; (k) Centric diatom from sample 13.

of the soil profiles (e.g., Alexandre et al. 1997; Blecker et al. 2006; Jones and Beavers 1963).

We applied a Phytolith Variation Index (PVI) to our dataset to explore depth-dependent losses and additions in phytolith concentrations and morphotypes relative to a reference collection (Cabanes et al. 2012). Sample 12 from the top of the core was assumed to be representative of the modern soil surface and used as the PVI reference. The PVI results can be divided into three groups (Figure 10). The first group was derived from the uppermost samples (12, 13, and 14), and the samples all had similar PVI values and phytolith concentrations. The second group derived from the middle of the core (15, 16, 17, 18, 19, and 20). These samples all had similar PVI, but different phytolith concentrations. We attribute these similar PVI values to an increase in dicotyledonous plant phytoliths found in these samples. The third group included samples 21 and 22, which had different PVI values between the two of them and between these samples and all others from the core. However, the major important aspects observed in these samples were the increase of C_3 grasses and dicot plants.

Hairs and sclereid phytoliths, which derive from dicotyledonous plant leaves, were found in the uppermost samples, but contrary to our expectations, not in lower samples where other dicot phytoliths were found. FTIR analysis also revealed that all of the samples shared a similar mineralogical composition, however, all samples were also lacking calcite. Therefore, we believe that the lack of specific morphotypes as well as the depth-dependent preservation of the phytoliths may be due to diagenetic processes that remain still unknown.

Translocation of phytoliths through sediments is an-

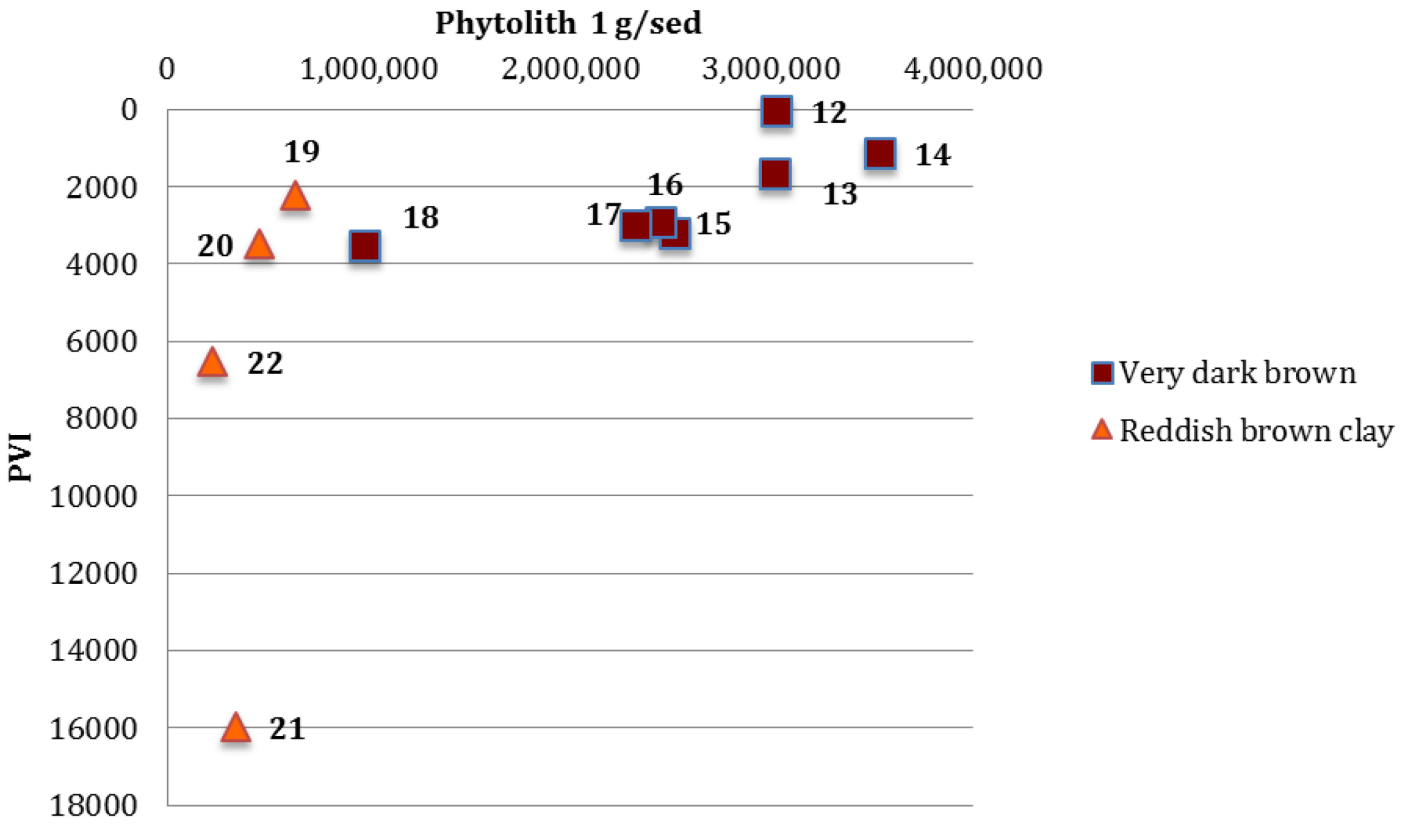

Figure 10. Plot of the PVI value for samples morphologically analyzed from Core C4.

other problem that has been observed in some terrestrial soil profiles (Alexandre et al. 1997; Fishkis et al. 2010; Fishkis et al. 2009; Piperno and Becker 1996). The transport rate of phytoliths can vary depending on the soil's physical properties (Fishkis et al. 2010). Our results showed that the phytolith coarse fraction was greatest in the lowermost stratums (YBC and OCS). Although few phytoliths in general were preserved in these strata, those remaining were mainly large bulliform cells or weathered and irregular shapes of big sizes (Figure 9I). Conversely, smaller phytoliths were rare in all samples, which may indicate translocation of these phytoliths to sediment depths below our sampling.

Phytolith Morphotypes

The phytoliths were divided into different groups depending on the type of the plant or the plant components where they were formed—monocotyledonous, grasses and leaves, and wood/bark of dicotyledonous plants. We identified a total of 37 different phytolith morphotypes, which are shown in Table 3. The phytolith distribution is shown in Figure 11. Samples from the lowest sedimentological stratums (23–28) were not included in the analysis because they exhibited low numbers of phytoliths not allowing for a reliable paleoenvironmental interpretation.

Grass phytoliths and phytoliths from monocotyledonous plants in general were the major component in all samples. Samples 12, 13, and 14 had the highest number of grass phytoliths (up to 50%), and these were primarily bulliform cells and prickles (~30%) that are characteristic of grass leaves (Figure 9A, -B, -C). Phytoliths from the Pooideae and Chloridoideae subfamilies were the only clear grass subfamilies identified, being represented by cylindroids rugulate and parallelepipeds elongate rugulate morphotypes (Figure 9F).

Monocotyledonous phytoliths predominated over typical grass phytoliths in samples 16–20. These include all those phytoliths, namely cylindroids rugulate and parallelepipeds elongate rugulate, which cannot be ascribed to any particular family due to their redundant morphologies (see Figure 9F).

Short cell bilobate morphotypes were also common (~15%) in the uppermost samples (Figure 9E; see Table 3). Twiss et al. (1969) and Twiss (1992), proposed a typological short cell classification associating bilobate and cross short cells to the C_4 Panicoideae subfamily, saddle short cells to the C_4 Chloridoideae subfamily and rondels, circular, oval or rectangular short cells to the C_3 Pooideae subfamily. However, the accuracy of this typology has been questioned by more recent findings showing that short cell rondel morphotypes, which would be typologically characteristic of C_3 grasses, are also found in East African C_4 grasses (Albert et al. 2006; Bamford et al. 2006; Barboni and Bremond 2009). Similarly, other studies have shown that bilobate short cells are produced in C_4 Panicoid grasses and some C_3 grasses (Cordova 2013; Cordova and Scott

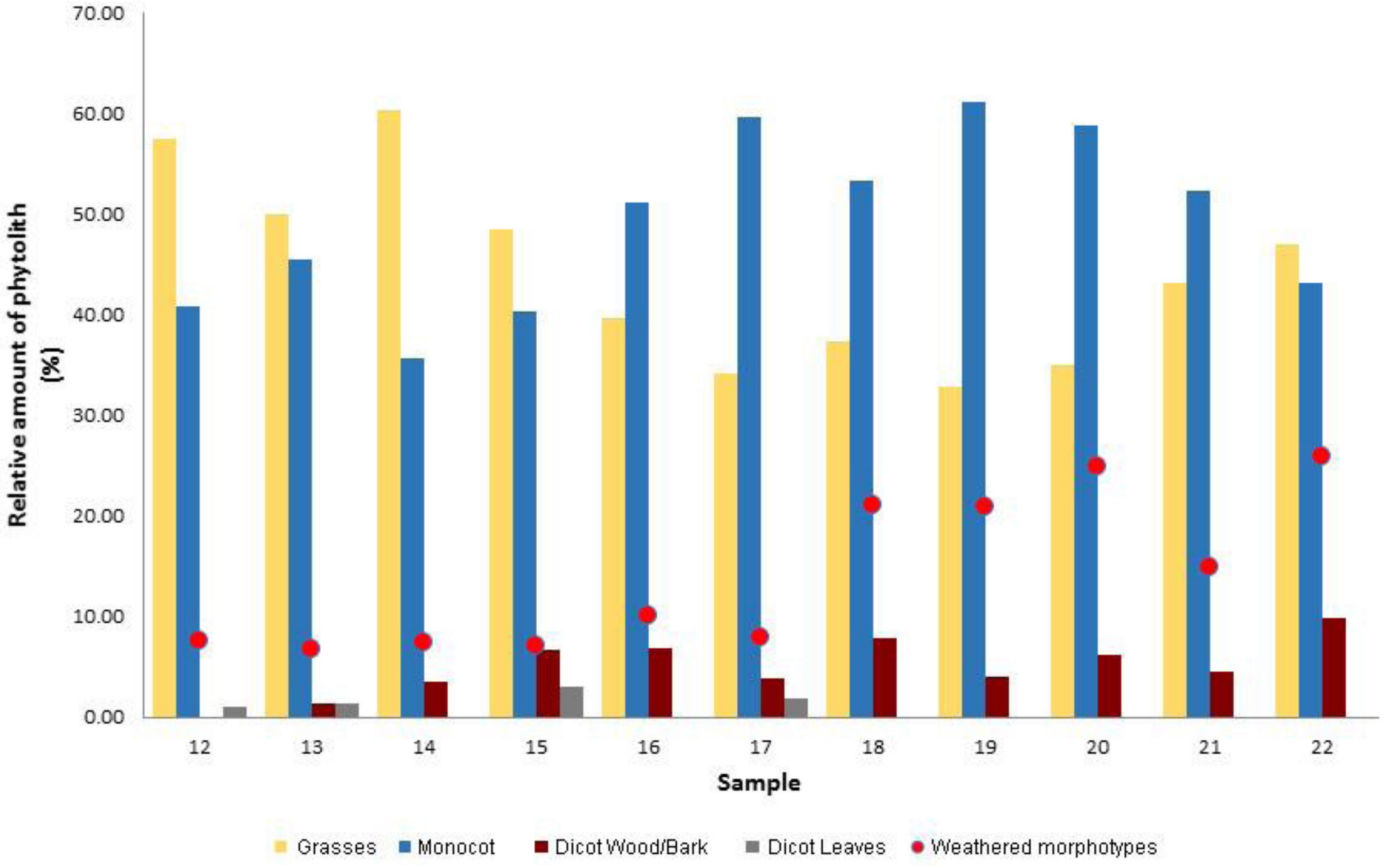

Figure 11. Histogram showing the phytolith morphological distribution from samples by the type of plant and the part of the plant identified (grasses, monocotyledonous plants, leaves and wood/bark of dicotyledonous plants) and weathered morphotypes.

2010; Piperno and Pearsall 1998; Rossouw 2009). Bilobate short cells therefore appear to be common in both C_3 and C_4. However, as they are produced in C_4 grasses in higher amounts, and the grasses currently growing in the area are mostly C_4 Panicoideae (mainly *Tristachya leucothrix* and *Loudetia simplex* among others) (Shackleton, 1991), we have assumed for the moment that short cell bilobate phytoliths come from C_4 Panicoideae grasses until further studies can be conducted.

Dicotyledonous phytoliths were also present in the samples, although in low numbers. Dicotyledonous plants are a paraphyletic group that includes flowering plants as well as woody / shrubby vegetation. The percentage of dicot phytoliths increased slightly (~9%) below layer 15 (see Table 3 and Figure 11). The most representative dicotyledonous phytolith morphotypes were ellipsoids rugulate, spheroids psilate and rugulate and parallelepipeds blocky (see Figure 9G). Sclereids, hairs, and platelets, diagnostic of the leaves of dicot plants, were also observed. Sclereid phytoliths branched shaped were identified only in sample 13. The hairs identified are small and all of them are curved (Figure 9H) and were identified only in samples 12, 15, and 17, all of them from the VDB stratum.

Large morphotypes like bulliform cells were more common in the lower samples. Increased frequencies of irregular morphotypes were also more common in the lower samples. Phytoliths with signs of dissolution were present in all the samples, but dissolution seemed to increase with depth (see Table 2).

Shackleton et al. (1991) described the climate of the Tongoland-Pondoland Mosaic as humid and the vegetation type as edaphic grasslands. Rosen and Weiner (1994) pointed to the higher silicification rates, and thus on phytolith production, noted in areas with abundant water availability and higher temperature of soils. Sangster and Parry (1969) also noted that grasses in locally wet habitats form high frequencies of bulliform morphotypes. Panicoid grasses mainly grow in warm environments with high available soil moisture (Tieszen et al. 1979; Twiss 1992). Moreover, Stromberg et al. (2007) pointed to the relationship between bulliform and short cell bilobates in humid environment. Thus, due to the high presence of short cell bilobates in all our samples together with the high presence of bulliform cells and diatoms (see Table 3), and taking into account the characteristics of the current vegetation of the area described by Shackleton et al. (1991), we hypothesized that at Pondoland the super production of bulliform cells would be indicative of a warm and humid environment.

TABLE 4. RADIOCARBON AGES FROM CORE C4.

Sample ID	^{14}C yr BP	$^{13}C/^{12}C$ Ratio (‰)	$^{13}C/^{12}C$ correction ^{14}C yr BP (1-sigma)	Calibrated age ranges, BP (INTCAL09)
15	460±30	-16.2	600±60	**660–540**
19	4440±30	-16.3	4580±30	**5440–5090**

Paleoenvironmental Reconstruction

Morphotypic changes in a phytolith assemblage can be used to model past local vegetation changes. Similarities across specific morphotypes allowed us to subdivide the C4 samples into three groups, representing different past environmental states.

Group 1. This was the most recent group and derived from samples 12–14. Grass phytoliths were most common, suggesting an open-habitat. Abundant short cell bilobate phytoliths suggest that the landscape may have been dominated by C_4 Panicoid grasses, which are also the predominant grass subfamily in the area today (Shackleton et al. 1991). However, morphological differences between the observed short cell bilobate morphotypes may be due to other grass species growing in the area. Phytoliths from dicotyledonous plants, as well as sclereids and hairs, were also noted in low quantities within this group. Based on these observations, Group 1 is interpreted to reflect an open-habitat landscape that was dominated by grasses with a minor component of discontinuous stands of trees and/or shrubs.

Group 2. This group is comprised of samples 15–20. These samples showed an increase in dicotyledonous phytoliths. The mix of grass and dicot phytoliths is interpreted to reflect a landscape that was characterized by semi-open vegetation, and dominated by a mixture of grassland and wooded/shrubby areas.

Group 3. Group 3 was composed of samples 21 and 22. Grass morphotypes were most common, being mainly trapeziform phytoliths. These morphotypes are exclusively ascribed to C_3 grasses (Barboni et al. 2007). These results are of major importance as they show an important vegetation flux from C_3 to C_4 grasslands. However, the low numbers of phytoliths make paleoenvironmental reconstructions difficult.

PALYNOLOGICAL ANALYSIS

Sediment core C4 was checked for palynomorphs. Palynomorphs were concentrated using 30% HCl, KOH, 48% HF, and acetolysis. Sodium polytungstate was used for heavy liquid separation. The residues were sieved over 10µm and 250µm mesh screens. The pollen samples were mounted in glycerol jelly. *Lycopodium* spores were added to all samples in order to calculate pollen and charred particle concentrations, which were expressed as the number of grains and fragments per gram sample. Identification and counting was performed with a light microscope under 400x and 1000x magnification.

RADIOCARBON ANALYSIS

Two bulk sediment samples from core C4 were sent to Beta-Analytic Inc. in Miami, FL for AMS radiocarbon dating (Table 4). The sediments were first floated and agitated in deionized H^2O to disperse the sediment. They were then progressively sieved thorough 250 and 180micron sieves to remove any plant macrofossils or rootlet material prior to the pretreatments. The <180µ size fraction was then subjected to a series of hot (near boiling) 0.5N HCl leaches to remove any carbonate presence. The samples were then rinsed with deionized H^2O until neutral and dried in a 70°C oven overnight. The pretreated sample material was then homogenized and inspected under a 45x microscope to inspect for any rootlet hairs or fragments, a portion was tested with acid again to insure that all carbonate had been removed. The sample was then combusted to CO^2 and graphitized for AMS counting. Quality control results were corrected for isotopic fractionation and measured against the NIST SRM-4990B standard. The AMS analysis of 4 reference materials were within 1-standard deviation relative to the NIST SRM-4990B reference standard

OSL DATING

Six sediment samples were submitted for OSL dating to the Luminescence Dating Laboratory at the University of Wollongong. The brief was to obtain range finder OSL ages for sediment samples collected from three different sites that was identified as being promising for future excavations of MSA deposits during a survey conducted of the area in 2011. OSL samples were only collected from archaeologically-sterile sedimentary deposits.

We used a combination of single aliquot and single grain OSL dating to obtain the range finder ages. Single aliquots were measured in the first place, followed by a more detailed investigation using single grains. The latter was deemed necessary, since all of the single aliquot data sets showed significant overdispersion in the measured equivalent dose (D_e) values. Using single grains, it is possible to explicitly investigate the potential causes of the observed overdispersion (e.g,. Jacobs 2005; Jacobs et al. 2006b; Jacobs and Roberts 2007). A single grain of sand is the smallest meaningful unit of measurement in OSL dating—which provides an estimate of the time elapsed since a grain was last exposed to sunlight—because each grain has experienced its own history of erosion, transport, and deposition. In contrast, when many grains are measured simultaneously as a composite aliquot, then grains of different ages may

be combined, giving an average age that may or may not be accurate. So, to avoid the confounding effect of dating potentially mixed-age components in composite samples, it is necessary to examine the distribution of equivalent dose (D_e) values from individual quartz grains; the D_e is the radiation energy absorbed by a quartz grain since it was last exposed to sunlight, and it can be estimated by measuring the OSL signal (Jacobs and Roberts 2007). From such data, it is possible to assess the stratigraphic integrity of a specific layer at a site. If all D_e estimates are statistically consistent with each other, then it can be safely inferred that the layer of interest has not been mixed. By contrast, the existence of a broad D_e distribution, or the presence of discrete populations of D_e values, indicates that the layer may contain mixed-age materials. Mixing may have occurred when the layer was formed originally (e.g., through the incorporation of reworked sediment grains from pre-existing deposits) or subsequently, via natural or anthropogenic processes of post-depositional disturbance (which could introduce both older and younger materials). In either case, the approach of dating individual grains of quartz provides the most reliable means of estimating the original time of deposition of a specific layer or unit and any associated archaeological items (Jacobs and Roberts 2007).

To investigate the burial ages of the Pondoland sediments from which samples were collected, we measured 24 single aliquots, where each aliquot contained ~20 grains of 180–212μm in diameter, and 1000 individual grains from each of the six samples collected.

Sample Collection

Six sediment samples were collected for OSL dating from three different sites—A3NW-8, B4NW-1, and C4NE-1. The samples were collected by E. Fisher and H. Cawthra who hammered plastic tubes, each about 5cm in diameter and 15cm long, into a cleaned section face at every chosen sample location. Additional sediment samples were also collected for laboratory measurements of the radioactivity present in the sediment and their present-day moisture content.

Sample Preparation

In the OSL dating laboratory at the University of Wollongong, the sample tubes were opened under dim red light. Sediment at both ends of each tube was discarded (as it would have contained grains exposed to sunlight at the time of sample collection), and quartz grains were then extracted from the light-safe portions using standard preparation procedures (Aitken 1998; Wintle 1997). First, all samples were wet sieved to isolate grains of 180–212μm in diameter. Second, carbonates still present in this fraction were dissolved in 10% hydrochloric acid and then organic matter was oxidized in 30% hydrogen peroxide solution. The remaining sample was dried and feldspar, quartz, and heavy minerals were separated by density separation using sodium polytungstate solutions of 2.62 and 2.70 specific gravities, respectively. The separated quartz grains were etched with 48% hydrofluoric acid for 40 min to remove the alpha-irradiated rind of each quartz grain and to destroy any remaining feldspars, and then rinsed in hydrochloric acid to remove any precipitated fluorides, dried and sieved again; grains retained on the 180μm diameter mesh were used for dating. We prefer the 180–212μm in diameter grain-size fraction for measurement of the equivalent dose to exploit the advantages and ease of single-grain measurements using standard equipment.

OSL Measurements

OSL measurements were made on multi-grain aliquots and individual grains of quartz. For multi-grain measurements, the 180–212μm in diameter grains were spread as a monolayer onto the surface of a stainless-steel disc after an area of 1mm in diameter was sprayed with silko-spray for the grains to adhere to; this amounts to ~20 grains per aliquot. Individual grains were measured using standard single grain discs that are 300μm in diameter and 300μm deep, containing 100 holes into which 200μm diameter grains are placed individually (Bøtter-Jensen et al. 2000).

All measurements were made in an identical manner and with the same equipment, using the single aliquot regenerative-dose (SAR) procedure described elsewhere (e.g., Jacobs et al. 2008a). The SAR procedure involves measuring the OSL signals from the natural (burial) dose and from a series of regenerative doses (given in the laboratory by means of a calibrated $^{90}Sr/^{90}Y$ beta source), each of which was preheated at 240°C for 10 s prior to optical stimulation by an intense, green (532 nm) laser beam for 2 s at 125°C in the case of single grains or by blue light emitting diodes (LEDs) for 40 s at 125°C. The resulting ultraviolet OSL emissions were detected by an Electron Tubes Ltd 9235QA photomultiplier tube fitted with Hoya U-340 filters. A fixed test dose (~10 Gy for single grains and 1.8 Gy for single aliquots, preheated at 160°C for 5 s) was given after each natural and regenerative dose, and the induced OSL signals were used to correct for any sensitivity changes during the SAR sequence. A duplicate regenerative dose was included in the procedure, to check on the adequacy of this sensitivity correction. As a check on possible contamination of the etched quartz grains by feldspar or other mineral-inclusions, we also applied the OSL IR depletion-ratio test (Duller 2003) to each grain and aliquot at the end of the SAR sequence, using an infrared exposure of 40 s at 50°C.

The D_e values for single grains were estimated from the first 0.22 s of OSL decay, with the mean count recorded over the last 0.3 s being subtracted as background, and for single aliquots the first 0.8 s and last 8 s of the OSL decay curve was used, respectively (Figure 12). The dose-response data were fitted using a linear or saturating exponential function, and the sensitivity-corrected natural OSL signal was projected on to the fitted dose-response curve to obtain the D_e by interpolation (Figure 13). The uncertainty on this estimate (from photon counting statistics, curve fitting uncertainties, and an allowance of 2% per OSL measurement for instrument irreproducibility) was determined by Monte Carlo simulation, using the procedures described by Duller (2007) and implemented in Analyst version 3.24. The final

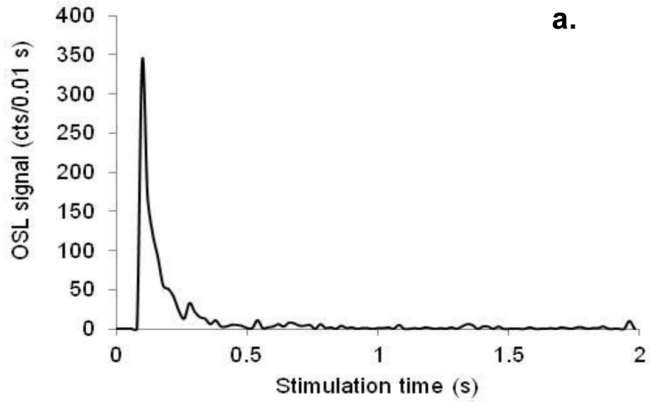

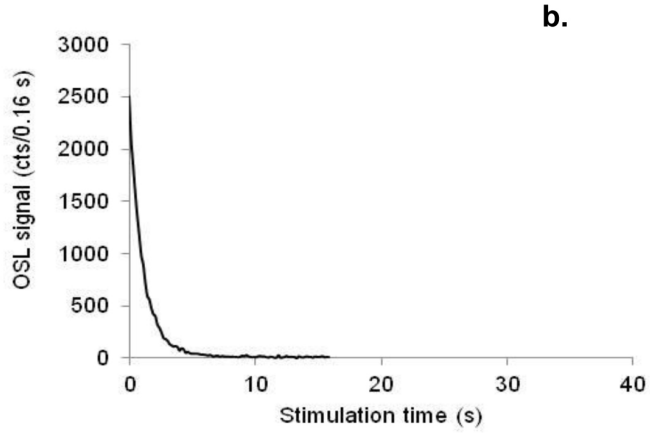

Figure 12. (a) A representative OSL decay curve for a moderately bright single-grain from sample EF5, and (b) a representative OSL decay curve for a single-aliquots from samples EF5.

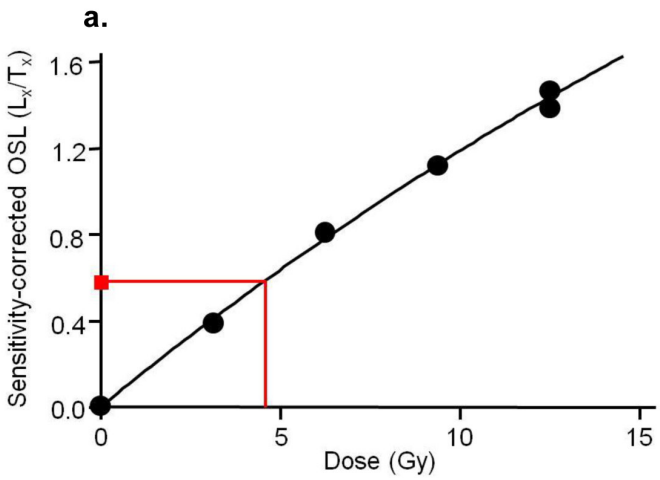

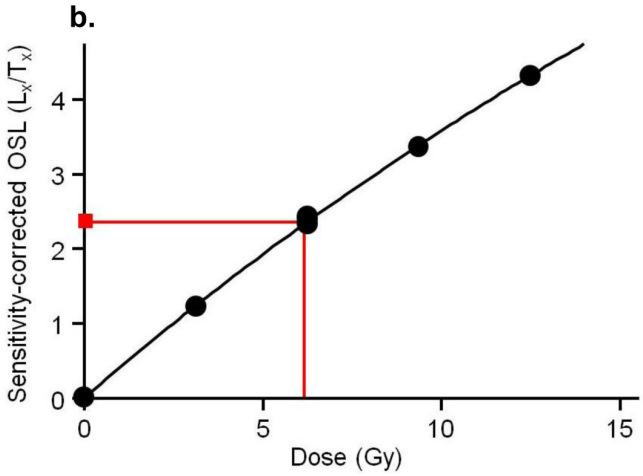

Figure 13. A representative dose response curve for same (a) single-grain and (b) single aliquot shown in Figure 12 from sample EF5.

age uncertainty includes a further 2% (added in quadrature) to allow for any bias in the beta source calibration. The $^{90}Sr/^{90}Y$ beta source was calibrated using a range of known gamma-irradiated quartz standards for both multi-grain aliquots and individual grain positions. Spatial variations in beta dose rate for individual grain positions were taken into account, based on measurements made using the same gamma-irradiated quartz standards (e.g., Ballarini et al. 2006).

Aberrant grains were rejected using the quality-assurance criteria described and tested previously (Jacobs et al. 2006a). Grains or aliquots were rejected if they exhibited one or more of the following properties: 1) weak test-dose OSL signals (i.e., the initial intensity of the test-dose signal was less than three times the background intensity and had a test dose error in excess of 30%); 2) poor recycling ratios (i.e., the sensitivity-corrected OSL values for duplicate regenerative doses differed by more than 2σ); 3) natural OSL signals equal to or greater than the saturation limit of the dose-response curve (i.e., the sensitivity-corrected natural OSL intensity exceeded that induced by the largest regenerative dose ['Class 3' grains of Yoshida et al. (2000)] or lay in the saturated region of the dose-response curve, so a finite estimate of D_e could not be obtained); and, 4) significant loss of OSL signal after exposure to infrared stimulation (i.e., the OSL IR depletion ratio was less than unity by more than 2σ, which indicates contamination of quartz grains by feldspar inclusions). Table 5 provides the details for all samples and the reasons for why single grains were rejected, respectively. No single aliquots were rejected.

Environmental Dose Rate Measurements And Results

The environmental dose rate is due mainly to beta and gamma radiation from the decay of ^{238}U, ^{235}U, ^{232}Th (and their daughter products) and ^{40}K in the deposits surrounding the dated grains. Beta dose rates were measured directly by low-level beta counting of dried, homogenized and powdered sediment samples in the laboratory, using a GM-25-5 multi-counter system (Bøtter-Jensen and Mejdahl 1988). Allowance was made for the effect of grain size and hydrofluoric acid etching on the beta dose rate, and a systematic uncertainty of 3% was included in the stan-

TABLE 5. NUMBER OF SINGLE-GRAINS MEASURED, REJECTED, AND ACCEPTED, TOGETHER WITH THE REASONS FOR THEIR REJECTION.

Sample name	No. of grains measured	T_N signal <3xBG	0 Gy dose >5% of L_N	Poor recycling ratio	No L_N/T_N intersection	Depletion by IR	Sum of rejected grains	Acceptable individual D_e values
EF1	1000	492	158	102	5	21	778	222
EF2	1000	766	39	50	21	33	909	91
EF3	1000	706	39	56	28	35	864	136
EF4	1000	469	170	138	0	26	803	197
EF5	1000	438	98	105	2	29	672	327
EF6	1000	388	117	105	1	19	630	370
	6000	**3259**	**621**	**556**	**57**	**163**	**4656**	**1343**

T_N is the OSL signal measured in response to the test dose given after measurement of the natural OSL signal.
L_N is the natural OSL signal.
Recycling ratio is the ratio of the sensitivity-corrected OSL signals measured from duplicate doses to test the efficacy of the test dose correction used in the SAR procedure.
IR is the infrared stimulation used to erase any part of the signal that may be derived from IR-sensitive (e.g., feldspar) grains.

dard error to the beta dose rate. To obtain an estimate of the gamma dose rate for the samples, the same dried, homogenized, and powdered sediments samples used for GM-25-5 beta counting were measured using thick source alpha counting (TSAC) to obtain estimates of uranium (U) and thorium (Th). Combining the results obtained from GM-25-5 beta counting and TSAC, an estimate of potassium (K) can be derived by subtraction. The estimates of U, Th, and K, so obtained, were then converted to gamma dose rates using the conversion factors of Guérin and Mercier (2011). This is not the preferred way of estimating the gamma dose rate. A superior way would be to estimate this directly in the field using a gamma spectrometer which would take into account any homogeneity in the ~30–40cm sphere surrounding the sediment sample. This should be done in any follow-up and detailed excavations of any of the sites.

An assumed effective dose rate of 0.032 Gy/ka was included for alpha emitters inside the quartz grains. The cosmic-ray dose rates were estimated following Prescott and Hutton (1994), taking into account the geomagnetic latitude and altitude of each of the sites, as well as the thickness and density of sediment (variable) and rock shielding each sample (averaged over the full period of burial). We assigned a relative uncertainty of 15% to account for the systematic uncertainty in the primary cosmic-ray intensity (Prescott and Hutton 1994), and uncertainties in our estimates of overburden. The beta, gamma, and cosmic-ray dose rates were calculated for long-term water contents. We used the current measured field values (of 3–11%) as representative and assigned a relative uncertainty of ±25% (at 1σ) to accommodate any likely variations over the burial period (Table 6).

The beta, gamma, and cosmic-ray dose rates were calculated for long-term water contents. The total dose rates for the six samples dated in this study range between 0.68±0.04 and 1.42±0.10 Gy/ka. Where more than one sample was collected from the same site, no obvious pattern of variation with depth or relative position in the site was observed (Table 6).

Equivalent Dose (D_e) Results And Age Estimates

Of the 144 single aliquots measured, all were used for final D_e determination. In contrast, of the 6000 individual grains measured, only 1343 grains (22.4% of the total number measured) were used for final D_e determination. Reasons for rejecting individual grains are provided in Table 6. Most grains (54.3% of the total number measured) were rejected because they were too dim following a laboratory dose (T_N signal<3xBG and/or T_N error >20%). Those grains that were accepted, however, had decay curves and dose response curves typical of quartz grains dominated by the most light-sensitive 'fast'-component (see FigureS 12 and 13), providing confidence in the accuracy of the resulting D_e estimates. The D_e values for all the accepted aliquots and grains are displayed as radial plots in the right and left-hand columns in Figure 14, respectively, for each of the samples. In such plots, the most precise estimates fall to the right and the least precise to the left. If these independent estimates are consistent with statistical expectations, then 95% of the points should scatter within a band of width ±2 units projecting from the left-hand ('standardized estimate') axis to any chosen D_e value on the right-hand, radial axis. The radial plot, thus, provides simultaneous information about the spread, precision, and statistical consistency of the D_e values (Galbraith 1988, 1990). It is immediately apparent from these plots that, for each of the samples, the D_e estimates are spread too widely to fall within any single band of ±2 units. This is also reflected in the D_e overdispersion values (see Table 6), which range from 38±3 (EF3) to 103±5% (EF1) for single grains and between 25±4 (EF6) and 59±9% (EF1) for the single aliquots. Overdispersion values up to ~20% are typical for samples globally that have been well-bleached prior to deposition and that remained undisturbed since burial (e.g., Arnold and Robert 2009; Olley et al. 2004). The range of overdispersion values for the samples from Pondoland thus suggests the possible presence of some or, in some cases, significant contamination.

To further investigate the spread in D_e values and the possible cause of contamination, suggested by the degree of overdispersion, we investigated the appearance of the radial plots shown in Figure 14. Explanations of the different general types of radial plot shapes that can be expected from typical processes that affect D_e distributions have been reviewed by Jacobs and Roberts (2007). Overall, the samples from sites A3NW-8 and C4NE-1 show distributions that are largely consistent with a central value, with some intrusion of older and younger grains, likely due to bioturbation. It has to be kept in mind that the majority of these samples were collected from natural erosional sections relatively close to the surface with evidence of modern vegetation that may disturb the sediments. We used the central age model (CAM) to provide a weighted mean age estimate that may or may not be meaningful. We argue that since these are only range-finder ages, the weighted mean ages will be skewed towards the age of the majority of grains, so the weighted mean age of both the single aliquots and single grains may approximate the true burial age of the sediments. Where discrete dose components are visible, we also applied the finite mixture model (FMM) following our standard approach (e.g., Jacobs et al. 2011; Jacobs et al. 2008b). We also used the information obtained from the radial plots and the age models to identify a D_e range that represents the majority of grains in any given sample, and used this as additional information to obtain our range-finder ages in samples that clearly did not remain undisturbed since burial.

Sample EF1 (A3NW-8)

Sample EF1 was collected from dark, organic-rich, archaeologically-sterile sediments in a natural exposure in front of the rock shelter. The sample is expected to provide a minimum age estimate for the archaeological sediments found within the shelter. This sample showed the highest overdispersion and its radial plot took on a shape that suggests a continuum of D_e values typical of what would be expected of a sample that have undergone mixing due to

TABLE 6. DOSE RATE DATA, EQUIVALENT DOSES, AND OSL AGES FOR SEDIMENT SAMPLES FROM PONDOLAND.

	Sample	Moisture content (%)	Dose rates (Gy/ka) Beta	Gamma	Cosmic	Total dose rate (Gy/ka)	D_e (Gy)	Age Model	Number of Grains	Over-dispersion (%)	Optical age (ka)
A3NW-8 (#36)	EF1 (SG)	11.7	0.54±0.04	0.49±0.03	0.1	1.16±0.08	2.07±0.15	CAM	222 / 1000	103±5	1.8±0.2
							1.0–3.7				0.85–3.2
	EF1 (SA)						3.00±0.36	CAM	24 / 24	59±9	2.6±0.4
B4NW-1 (#44)	EF2 (SG)	9.2	0.30±0.02	0.28±0.02	0.07	0.68±0.04	146.8±7.6	CAM	91 / 1000	41±4	216±19
							203.0±8.2	FMM-1			***300±24***
							97.6±6.2	FMM-2			144±13
	EF2 (SA)						177.2±12.0	CAM	21 / 24	27±5	262±25
B4NW-1 (#46)	EF3 (SG)	3.3	0.27±0.02	0.32±0.02	0.07	0.68±0.05	90.6±2.8	CAM	94 / 1000	38±3	***133±11***
	EF3 (SA)						113.8±8.3	CAM	24 / 24	34±5	166±17
C4NE-1 (#5)	EF4 (SG)	7.4	0.58±0.03	0.42±0.03	0.07	1.10±0.07	2.04±0.12	CAM	197 / 1000	73±4	1.9±0.2
							1.4–3.1	Range			1.2–2.8
	EF4 (SA)						2.08±0.18	CAM	24 / 24	42±6	1.9±0.2
C4NE-1 (#6)	EF5 (SG)	6.2	0.68±0.04	0.69±0.06	0.02	1.42±0.10	4.93±0.15	CAM	327 / 1000	53±2	3.5±0.3
							3.5–4.7	Range			2.4–3.3
	EF5 (SA)						6.00±0.33	CAM	24 / 24	27±4	4.2±0.4
C4NE-1 (#7)	EF6 (SG)	5.7	0.78±0.04	0.55±0.03	0.02	1.37±0.08	4.60±0.09	CAM	370 / 1000	43±2	3.3±0.2
							4.0–6.8	Range			2.9–5.0
	EF6 (SG)						5.45±0.28	CAM	24 / 24	25 ± 4	3.9±0.3

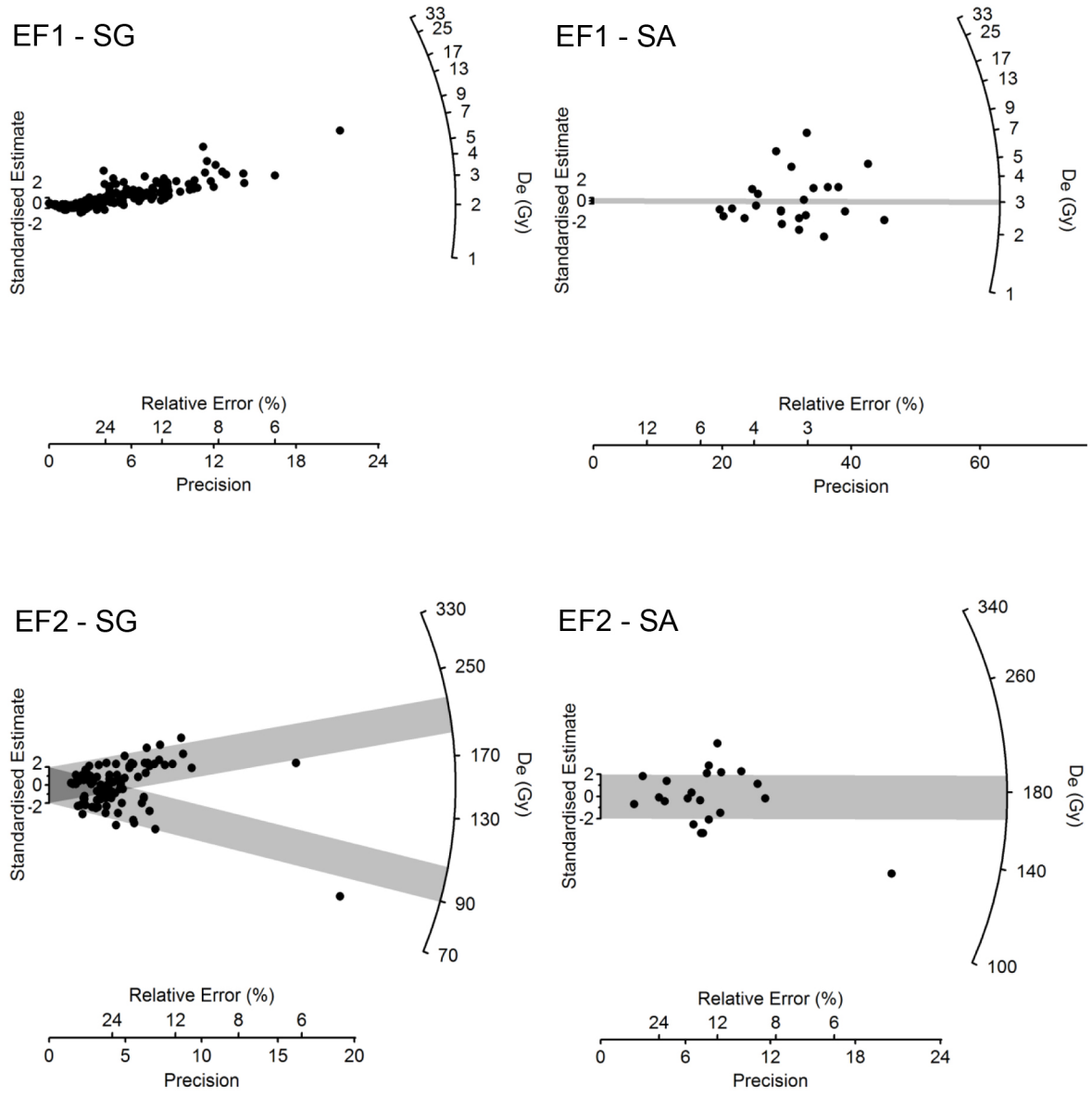

Figure 14 (shown in three sections). Radial plots of single-grain (left column) and single aliquot (right column) De values for all six samples measured in this study. The grey bar is centered on the weighted mean De value, except for EF2 for which the FMM was used.

bioturbation. What cannot be seen from the radial plot is the amount of 'modern' grain contamination. Out of the 222 grains for which D_e values were obtained, 37 grains, or ~17% of the calculated D_e values, were 'zero' or 'negative.' When the finite mixture model is applied to this sample, the model did not converge on an optimal value, so no discrete D_e components could be obtained, which also supports our interpretation that this sample likely suffered from bioturbation. But what we could glean from the results is that ~70% of the grains are consistent with D_e values of between ~1 and ~3.8 Gy. In other words, despite the presence of both younger and older grains, there are a large number of grains that fall in this bracket. When taking into account the environmental dose rate for this sample (see Table 6), an age bracket of between ~850 and 3200 years can, thus, be established for the majority of the grains in this sample. Both the weighted mean ages obtained from the single grains and single aliquots of ~1800 and 2600 years, respectively, are consistent with this age bracket. It is thus likely that the archaeological-bearing sediments inside the shelter are at least ~3200 years old, which would be consistent with a Wilton-age assemblage that dates to between 4 and 8 ka elsewhere in South Africa, and that was identified from surficial lithic scatters in the shelter (see discussion of A3NW-8 in main text).

Samples EF2 And EF3 (B4NW-1)

Samples EF2 and EF3 were collected from the same site (B4NW-1), but from different sedimentary facies. Sample EF3 was collected from Facies 2 an upper paleosol unit that, in places, clearly truncated the underlying Facies 1, the lower paleosol, from which sample EF2 was collected.

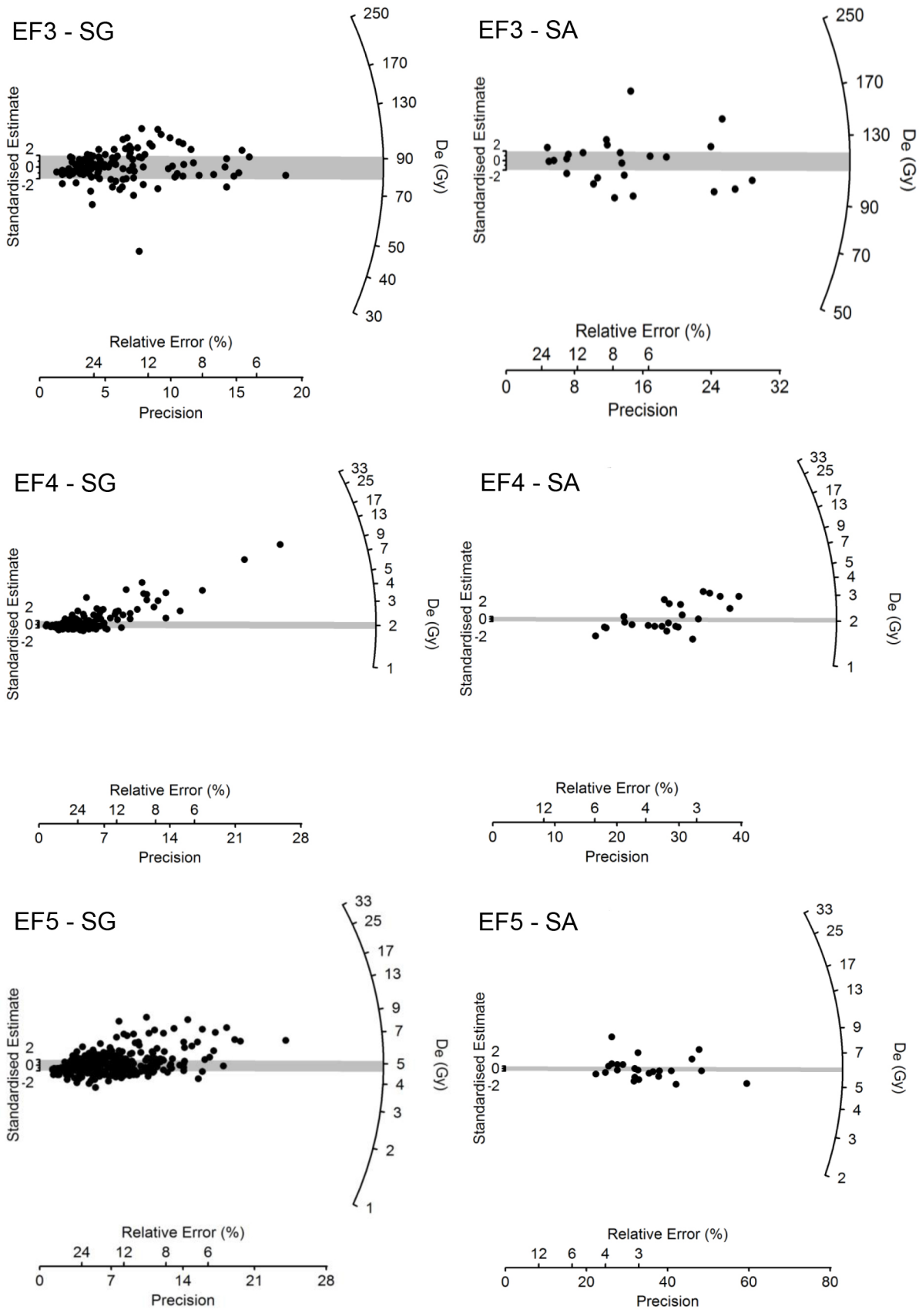

Figure 14 (shown in three sections) continued.

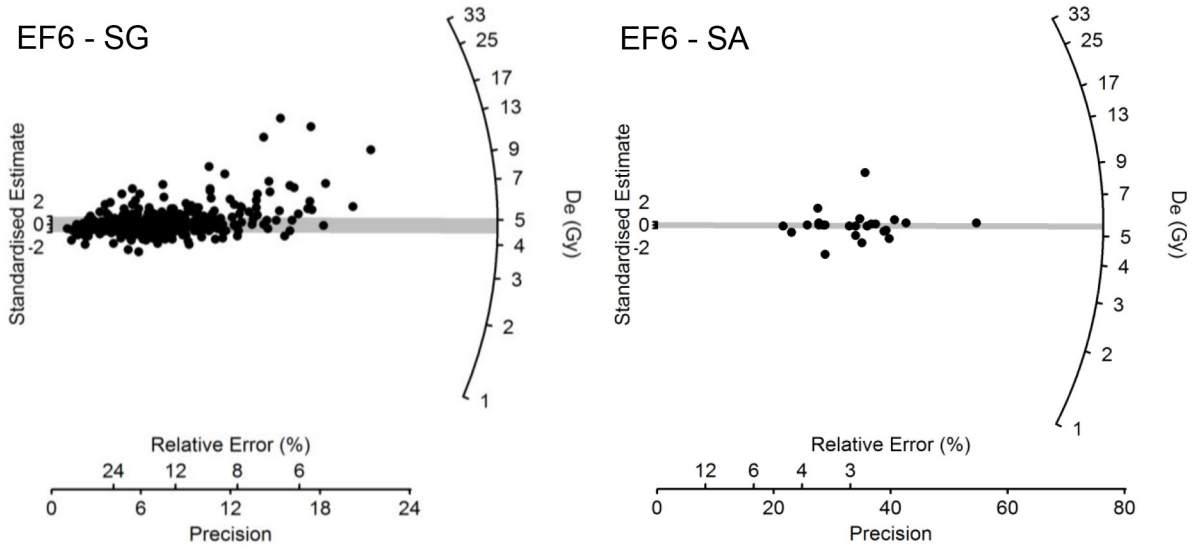

Figure 14 (shown in three sections) continued.

The single grain radial plots (see Figure 14) show two very different patterns for the two samples. EF2 shows a clearly bi-modal distribution, whereas EF3 shows a broader and more continuous distribution, with the exception of a few low D_e values. We applied the FMM to the D_e dataset for EF2 to obtain the weighted mean and proportion for each of the two discrete D_e components. The FMM converged on an optimal combination of values (see Jacobs et al. 2011; Jacobs et al. 2008b for explanations) when two components were fitted, each with an overdispersion value of 12%. The major component, represented by 64% of the grains gave an age of 300±24 ka and the minor component, represented by 36% of the grains, gave an age of 144±13 ka.

Due to the limited lateral shoreline shifts on this narrow continental shelf, east coast dune systems tend to accrete vertically, rather than penetrating far inland (Cawthra et al. 2012; Porat and Botha 2008). Climate along the South African east coast is most significantly influenced by the presence of the Agulhas Current, which follows a trajectory along the continental shelf break (Lutjeharms 2006), approximately 8km from the present shoreline. The east coast becomes more tropical northward, falling latitudinally within the sub-tropical zone, with dominant summer rainfall (Taljaard 1996). Precipitation is derived from both (winter) cyclonic and (summer) anticyclonic weather systems. The sub-tropical climate in the study region accelerates erosional and weathering processes as deep weathering associated with this climate pattern has partially obscured primary sedimentary features of Late Cenozoic successions. Botha and Porat (2007) have documented dominant chemical changes to East Coast solumn via soil degradation, erosion, and vegetation cover.

The resultant manifestation of the above processes is evident in the OSL samples from site B4NW-1. A bimodal age distribution within sample number 44 reflects particle mixing as a result of erosion in the surface and sub-surface layers of this unit. Sample 44 (from facies 1) stratigraphically underlies the dated facies 2 (sample 46). Incised gullies in the outcrop attributed to rainwater flow over a relatively steep slope have likely disrupted the uppermost stratigraphy in these deposits.

The FMM did not converge on an optimal value when applied to the EF3 data set. This means that there are no finite and discrete D_e components that can be statistically separated, as can clearly be seen from the radial plot. About 90% of the grains in this sample are consistent with D_e values ranging between ~82 and 130 Gy, which, when divided by its total environmental dose rate (see Table 2), results in an age range of between ~120 and 190 ka. This range encompasses the weighted mean ages of 133±11 and 166±17 ka calculated from the single grain and single aliquot data sets, respectively (see Table 6). Furthermore, the age of this sample is also consistent with the age of the minor age component identified for the sample (EF2) collected from the underlying Facies 1 unit, supporting the field observations that the upper paleosol unit has truncated the lower paleosol in places, resulting in some mixing of the two facies. Our best age estimates for the two units sampled at this site is, therefore, ~300 ka for the lowermost Facies 1 and somewhere between 130 and 190 ka for Facies 2. Both facies predate the last interglacial (MIS5e).

Samples EF4, EF5, And EF5 (C4NE-1)

Samples EF4, EF5 and EF6 were collected from sterile sediments within natural exposures in front of site C4NE-1. The samples targeted different strata seen within the sections. The samples were expected to provide minimum age estimates for the archaeological sediments.

The radial plots of all three samples show similar patterns. The majority of the grains have D_e values that are self-consistent, but there is also a tail of older grains that contaminate each of the samples. In sample EF4, ~86% of

the grains are consistent with the range presented in Table 6, ~70% of the grains in EF5, and ~96% of the grains in EF6. This domination of grains with a tight range in D_e values also explains why there is such good agreement between the single grain and single aliquot ages. Our best estimate range-finder ages for these three samples are ~2000 years for sample EF4, and ~3500–4000 years for both EF5 and EF6.

Conclusions

The final ages for all six samples are listed in Table 6, together with the supporting D_e and dose rate estimates. Uncertainties on the ages are given at 1σ (standard error of the mean) and were derived by combining, in quadrature, all known and estimated sources of random and systematic error. For the sample D_e, the random error was obtained from the model used to determine the weighted mean (i.e., CAM or FMM), and a systematic error (of 2%) was included for any possible bias associated with calibration of the laboratory beta source. The total uncertainty on each dose rate was obtained as the quadratic sum of all random (measurement) errors and the systematic errors associated with estimation of the beta and cosmic-ray dose rates. The ages range from as little as <1000 years to as much as 300,000 years, clearly showing the potential time-depth represented by the sites surveyed in Pondoland.

TERRESTRIAL FAUNA

Photographs of surficial terrestrial fauna were taken at every site using a Nikon D300s and 18-200 Nikon Nikkor DX 18–200mm f3.5–5.6GII lens. Specimens were placed onto a 1cm grid and photographed at highest resolution (NEF); 50% grey, 18% grey, white, and black patches on the grid assisted in correcting systematic color shift and exposure.

These photographs are included as part of site descriptions in SOM-S2. The terrestrial fauna species identification was done on the basis of these photographs and Table 7 summarizes the results. It is assumed that the photographed assemblage was not exhaustive and it could be biased towards larger and/or visible faunal remains.

MARINE FAUNA

Photographs of surficial shellfish specimens were taken at every site using a Nikon D300s and 18-200 Nikon Nikkor DX 18–200mm f3.5–5.6GII lens. Specimens were placed onto a 1cm grid and photographed at highest resolution (NEF); 50% grey, 18% grey, white, and black patches on the grid assisted in correcting systematic color shift and exposure.

These photographs are included as part of site descriptions in SOM-S2. The shellfish species identification was done on the basis of these photographs and is summarized in Table 8. It is assumed that the photographed assemblage was not exhaustive and it could be biased towards larger and/or visible shells.

Thirty-six categories of invertebrates are documented (see Table 8): twenty-eight to species level, three to genus level, two to Family level, one to class level, and two to vernacular mollusk names (whelks unidentified, land gastropods), within which, an entire order and a subclass fit in, respectively. One taxon identified to species level is a crustacean (*Octomeris angulosa*) that lives mostly on rocks but at times also on top of shellfish that live on the same substrate. There are no species out of their current geographic range represented.

The taxa that are most frequently represented are several limpets from the genus *Cymbula* and *Scutellastra*, the rocky shore bivalve *Perna perna*, a few whelk species from the genus *Burnupena* and turban snails (*Turbo coronatus* and *Turbo cidaris natalensis*). Most of them were collected from the mid-intertidal to lower intertidal, found on and among rocks, and at times also in pools. The same applies to other and less represented species appearing in Table 8, although *Tivela polita* burrows in fine, clean sand just below low tide on high energy beaches. Interestingly, the habitat requirements of the Natal rock oyster (*Sacostrea cuccullata*) are flexible enough as to form a conspicuous belt on the upper mid-tidal, settle wave washed rocks platforms and also enter estuaries where it can tolerate low salinities and settle on other shells and mangrove roots (Kilburn and Rippey 1982). Several marine mollusks (*Cymbula miniata*, *C. sanguinans*, *Scutellastra barbara*, *S. argenvillei*, *S. pica*, *S. cochlear*, *Charonia lampas pustula*, *Fusinus* sp.) were probably collected during low tides, such as monthly spring low tides, due to their distribution in the lower intertidal and shallow subtidal (Branch et al. 2010). *Scutellastra tabularis* is a subtidal species, however, the photographed specimens are young adults which also can be collected in the low intertidal (personal observation). Of note is also that half of the recorded *S. cochlear* are sub-adults. These often live on top of adults until they can find free rock space to settle (Branch and Branch 1992). Hence, their inclusion in archaeological contexts probably resulted from the collection of adult specimens. Land gastropods could be found either on terrestrial or fresh water environments.

Some species (cowries and *Nerita albicilla*) were probably collected for purposes other than dietary given their small flesh yield and known use as ornaments among southern African indigenous people today and during LSA times (Mitchell 1996). Cowries occur intertidally on rocks or under stones in pools, and *N. albicilla* lives in similar environs and is the most common nerite in southern African shores (Branch et al. 2010). Likewise, normally small sized keyhole limpets, such as the one recorded here (*Dedrofissurella scutellum*), could also have been collected for decorative purposes. This species in particular seems to contain toxins that must make it inedible (Branch et al. 2010).

REFERENCES

Aitken, M.J. 1998. *Introduction to optical dating*. Oxford University Press, New York.

Albert, R.M., Bamford, M.K., and Cabanes, D. 2006. Taphonomy of phytoliths and macroplants in different soils from Olduvai Gorge (Tanzania) and the application to Plio-Pleistocene palaeoanthropological samples. *Quaternary International* 148: 78–94.

TABLE 7. DETAILS OF EACH OF THE PHOTOGRAPHED FAUNA SPECIMENS FROM THE SURVEY.

Site	Figure	Figure Element	General Description	Age	Family	ID	Size Class
A2SE-1	2-3	A	Unidentifiable frag				
A2SE-1	2-3	B	Unidentifiable shaft frag				Size 2
A2SE-1	2-3	C	Unidentifiable frag				
A2SE-1	2-3	D	Unidentifiable frag				Size 2
A2SE-1	2-3	E	Astragalus		Bovid		Size 2
A2SE-1	2-3	F	Unidentifiable shaft frag				Size 2
A2SE-1	2-3	G	Unidentifiable frag				Size 2
A2SE-1	2-3	H	Unidentifiable shaft frag				Size 2
A2SE-1	2-3	I	Tooth		Bovid/ Equid		Size 4
A2SE-1	2-3	J	Mandible		Bovid		Size 1
A2SE-1	2-3	K	Mandible		Bovid		Size 2
A3NW-7A	2-16	A	Unidentifiable shaft frag				
A3NW-7A	2-16	B	Unidentifiable shaft frag				
A3NW-7A	2-16	C	R. Mandible		Leporidae	*Lepus saxatilis* ?	Size 1
A3NW-7A	2-16	D	Unidentifiable frag				
A3NW-7A	2-16	D	Unidentifiable frag				Size 1
A3NW-7A	2-16	D	Unidentifiable frag				
A3NW-7A	2-16	D	Unidentifiable frag				
A3NW-7A	2-16	D	Unidentifiable shaft frag				
A3NW-7A	2-16	D	Unidentifiable shaft frag				
A3NW-7A	2-16	D	Unidentifiable shaft frag				Size 1
A3NW-7A	2-16	D	Unidentifiable shaft frag				Size 1
A3NW-7A	2-16	D	Unidentifiable shaft frag				Size 1
A3NW-7A	2-16	D	Unidentifiable shaft frag				
A3NW-7A	2-16	D	Unidentifiable shaft frag				Size 1
A3NW-8	2-23	A	R. Astragalus		Bovid		Size 4
A3NW-8	2-23		Humerus				Size 1
A3NW-8	2-23		Unidentifiable frag				
A3NW-8	2-23		Unidentifiable shaft frag				
A3NW-8	2-23		Unidentifiable shaft frag				Size 2
A3NW-8	2-23		Unidentifiable shaft frag				Size 2
A3NW-8	2-23		Unidentifiable shaft frag				Size 2
A3NW-8	2-23		Unidentifiable shaft frag				Size 2
A3NW-8	2-23		Unidentifiable shaft frag				Size 2
A3NW-9	2-46	A	L. Acetabalum		Equid		Size 4
A3NW-9	2-46	B	Unidentifiable shaft frag				Size 2
A3NW-9	2-46	C	R. Femur	Adult	Leporidae	*Lepus saxatilis*	
A3NW-9	2-46	D	Unidentifiable frag				

TABLE 7. DETAILS OF EACH OF THE PHOTOGRAPHED FAUNA SPECIMENS FROM THE SURVEY (continued).

Site	Figure	Figure Element	General Description	Age	Family	ID	Size Class
B3SE-2	2-55	A	Metapodial	Adult	Bovid		Size 3
B3SE-2	2-55	B	Unidentifiable frag				
B3SE-7	2-83	A	Unidentifiable frag				Size 2
B3SE-7	2-83	B	L. Maxilla	Adult	Suid		Size 2
B3SE-4	2-65	B	Tooth fragment		Bovid		Size 2
B3SE-4	2-65	A	Tooth fragment		Bovid		Size 2
B3SE-4	2-65	C	Tooth fragment				
B3SE-4	2-65		Unidentifiable frag				
B3SE-4	2-65		Unidentifiable frag				
B3SE-4	2-65		Unidentifiable shaft frag				
B3SE-4	2-65		Unidentifiable shaft frag				
B3SE-4	2-65		Unidentifiable shaft frag				
B3SE-8	2-92	A	R. Femur	Adult	Leporidae	*Lepus saxatilis* ?	Size 1
B3SE-8	2-92		Unidentifiable frag				
B3SE-8	2-92		Unidentifiable shaft frag				
B4NE-1	2-102	A	Tibia		Bovid		Size 2
B4NE-1	2-102	B	Vertebrae				Micro-mammal
B4NE-1	2-102		Unidentifiable frag				
C4NE-1	2-126	A	Metatarsal	Adult	Bovid		Size 3
C4NE-1	2-126	B	R. Mandible		Suid		Size 2
C4NE-1	2-126	C	Premolar		Bovid		
C4NE-1	2-126	D	R. Humerus	Adult	Bovid		Size 2
C4NE-1	2-126	E	L. Scapula	Adult	Bovid		
C4NE-1	2-126	F	Phalanx		Bovid		Size 4
C4NE-1	2-126	G	Ulna	Adult	Bovid		Size 4
C4NE-1	2-126	H	Unidentifiable frag				
C4NE-1	2-126	I	Ulna	Adult	Leporidae	*Lepus saxatilis*	
C4NE-1	2-126	J	L. Femur	Adult	Leporidae	*Lepus saxatilis*	
C4NE-2	2-137	A	L Tibia ?	Adult	Equid		Size 4
C4NE-2	2-137	B	C. Vertebrate		Bovid		Size 2
C4NE-2	2-137	C	Metapodial (likely a metacarpal)	Adult	Bovid		Size 2
C4NE-2	2-137	D	L. Innominate	Adult	Canid		Size 1
C4NE-2	2-137	E	C. Vertebrate	Adult	Bovid		Size 2
C4NE-2	2-137	F	Innominate	Adult			Size 1
C4NE-2	2-137	G	L. Humerus	Adult	Felid		Size 1
C4NE-2	2-137	H	Skull		Leporidae	*Lepus saxatilis*	Size 1

TABLE 8. PRESENCE (indicated with an X) OF INVERTEBRATE SPECIES OBSERVED IN COASTAL SURVEYED SITES IN PONDOLAND, SOUTH AFRICA.

		Archaeological Sites													
Common name	**Scientific name**	**A2SE-1**	**A3NW-7**	**A3NW-1**	**A3NW-8**	**A3NW-9**	**B3SE-2**	**B3SE-3**	**B3SE-4**	**B3SE-7**	**B3SE-8**	**B4NE-1**	**C4NE-1**	**C4NE-2**	**C4SW-1**
Chitons	*Dinoplax validifossus*									x				x	**x**
	Poliplacophora (Class)					x									
Cowries	*Cypraea annulus* *					x			x						
	Cypraea sp *													x	
Limpets	*Cymbula miniata*	x			x						x				
	Cymbula sanguinans		x		x	x	x	x	x		x	x	x		**x**
	Cymbula oculus	x	x		x	x	x				x		x		**x**
	Scutellastra barbara								x		x				
	Scutellastra argenvillei	x		x				x							
	Scutellastra granularis		x											x	
	Scutellastra longicosta		x							x		x			
	Scutellastra pica							x			x				
	Scutellastra tabularis			(x)		(x)	(x)			(x)			(x)	(x)	**(x)**
	Scuttelastra cochlear	x	(x)	x	(x)	x	(x)	(x)		x	(x)			x	**(x)**
	Cellana capensis										x				
Abalone	*Haliotis spadicea*						x					x			
Keyhole limpet	*Dedrofissurella scutellum*									x					
Mussel	*Perna perna*	x	x	x	x	x		x	x	x	x		x		
Oyster	*Sacostrea cucullata*						x						x	x	
	Ostreidae (Family)						x					x			

Asterisk (*) denotes species collected most likely for non-dietary purposes. Presence of species in parenthesis (X) indicates sub-adults.

TABLE 8. PRESENCE (indicated with an X) OF INVERTEBRATE SPECIES OBSERVED IN COASTAL SURVEYED SITES IN PONDOLAND, SOUTH AFRICA (continued).

		Archaeological Sites													
Common name	**Scientific name**	**A2SE-1**	**A3NW-7**	**A3NW-1**	**A3NW-8**	**A3NW-9**	**B3SE-2**	**B3SE-3**	**B3SE-4**	**B3SE-7**	**B3SE-8**	**B4NE-1**	**C4NE-1**	**C4NE-2**	**C4SW-1**
Sand clam	*Tivela polita*	x													
Turban snails	*Turbo cidaris natalensis*						x				x				
	Turbo coronatus	x					x				x	x	x		
Whelks	*Burnupena pubescens*					x				x	x				
	Burnupena lagenaria		x	x					x						
	Burnupena cincta			x	x										
	Burnupena sp.												x		
	Charonia lampas pustula		x		x		x						x		
	Fusinus sp.			x											
	Argobuccinum pustulosum				x										
	Thais capensis												x		
	Nerita albicilla *						x								
	Muricidae (Family)		x												
	Whelk unidentif.				(x)										
Terrestrial/ fresh water gastropod	Land gastropods	x					x								
Barnacle	*Octomeris angulosa*						x								

Asterisk (*) denotes species collected most likely for non-dietary purposes. Presence of species in parenthesis (X) indicates sub-adults.

Albert, R.M., Esteve, X., Portillo, M., Rodríguez-Cintas, A., Cabanes, D., Esteban, I., and Hernández, F. 2011. Phytolith CoRe, Phytolith Reference Collection, Extraído Septiembre, 2012.

Albert, R.M. and Weiner, S. 2001. Study of phytoliths in prehistoric ash layers using a quantitative approach. In *Phytoliths: Applications in Earth Sciences and Human History*, Meunier, J.D. and Colin, F. (eds.). Balkema Publishers, Lisse, pp. 251–266.

Alexandre, A., Meunier, J.D., Lezine, A.M., Vincens, A., and Schwartz, D. 1997. Phytoliths: indicators of grassland dynamics during the late Holocene in intertropical Africa. *Palaeogeography Palaeoclimatology Palaeoecology* 136(1–4): 213–229.

Arnold, L.J. and Robert, R.G. 2009. Stochastic modelling of multi-grain equivalent dose (D_e) distributions: implications for OSL dating of sediment mixtures. *Quaternary Geochronology* 4: 204–230.

Ballarini, M., Wintle, A.G., and Wallinga, J. 2006. Spatial variation of dose rates from beta sources as measured using single grains. *Ancient TL* 24: 1–8.

Bamford, M.K., Albert, R.M., and Cabanes, D. 2006. Plio-Pleistocene macroplant fossil remains and phytoliths from Lowermost Bed II in the eastern palaeolake margin of Olduvai Gorge, Tanzania. *Quaternary International* 148: 95–112.

Barboni, D. and Bremond, L. 2009. Phytoliths of East African grasses: An assessment of their environmental and taxonomic significance based on floristic data. *Review of Palaeobotany and Palynology* 158(1–2): 29–41.

Barboni, D., Bremond, L., and Bonnefille, R. 2007. Comparative study of modern phytolith assemblages from inter-tropical Africa. *Palaeogeography Palaeoclimatology Palaeoecology* 246(2–4): 454–470.

Blecker, S.W., McCulley, R.L., Chadwick, O.A., and Kelly, E.F. 2006. Biologic cycling of silica across a grassland bioclimosequence. *Global Biogeochemical Cycles* 20(3): 1–11.

Botha, G. and Porat, N. 2007. Soil chronosequence development in dunes on the southeast African coastal plain, Maputaland, South Africa. *Quaternary International* 162: 111–132.

Bøtter-Jensen, L., Bulur, E., Duller, G.A.T., and Murray, A. 2000. Advances in luminescence instruments systems. *Radiation Measurements* 32: 523–528.

Bøtter-Jensen, L. and Mejdahl, V. 1988. Assessment of beta dose-rate using a GM multicounter system. *Nuclear Tracks and Radiation Measurements* 14: 187–191.

Branch, G.M. and Branch, M. 1992. *The living shores of Southern Africa*. Struik Publishers, Cape Town.

Branch, G.M., Griffiths, C.L., Branch, M.L., and Beckley, L.E. 2010. *Two Oceans: A Guide to the Marine Life of Southern Africa*. D. Philip, Cape Town.

Cabanes, D., Gadot, Y., Cabanes, M., Finkelstein, I., Weiner, S., and Shahack-Gross, R. 2012. Human impact around settlement sites: a phytolith and mineralogical study for assessing site boundaries, phytolith preservation, and implications for spatial reconstructions using plant remains. *Journal of Archaeological Science* 39(8): 2697–2705.

Cawthra, H.C., Uken, R., and Ovechkina, M. 2012. New insights into the geological evolution of the Bluff Ridge and adjacent Blood Reef, Durban, South Africa. *South African Journal of Geology* 115(3): 291–308.

Cordova, C.E. 2013. C3 Poaceae and Restionaceae phytoliths as potential proxies for reconstructing winter rainfall in South Africa. *Quaternary International* 287(0): 121–140.

Cordova, C.E. and Scott, L. 2010. The potential of Poaceae, Cyperaceae, and Restionaceae phytoliths to reflect past environmental conditions in South Africa. In *African Palaeoenvironmental and Geomorphic Landscape Evolution*, Runge, J. (ed.), Taylor and Francis, Boca Raton, pp. 107–133.

Duller, G.A.T. 2003. Distinguishing quartz and feldspar in single grain luminescence measurements. *Radiation Measurements* 37(2): 161–165.

Duller, G.A.T. 2007. Assessing the error on equivalent dose estimates derived from single aliquot regenerative dose measurements. *Ancient TL* 25: 15–24.

Fishkis, O., Ingwersen, J., Lamers, M., Denysenko, D., and Streck, T. 2010. Phytolith transport in soil: A field study using fluorescent labelling. *Geoderma* 157(1–2): 27–36.

Fishkis, O., Ingwersen, J., and Streck, T. 2009. Phytolith transport in sandy sediment: Experiments and modeling. *Geoderma* 151(3–4): 168–178.

Galbraith, R. 1988. Graphical display of estimates having different standard errors. *Technometrics* 30: 271–281.

Galbraith, R. 1990. The radial plot: graphical assessment of spread of ages. *Nuclear Tracks and Radiation Measurements* 17: 207–214.

Guérin, G. and Mercier, N. 2011. Determining gamma dose rates by field gamma spectroscopy in sedimentary media: Results of Monte Carlo simulations. *Radiation Measurements* 46(2): 190–195.

Jacobs, Z. 2005. Testing and demonstrating the stratigraphic integrity of artefacts from MSA deposits at Blombos Cave, South Africa, in: d'Errico, F., Backwell, L. (eds.), *From tools to symbols: from early hominids to modern humans*. Witwatersrand University Press, Johannesburg, pp. 459–474.

Jacobs, Z., Duller, G.A.T., and Wintle, A.G. 2006a. Interpretation of single grain D_e distributions and calculation of D_e. *Radiation Measurements* 41(3): 264–277.

Jacobs, Z., Duller, G.A.T., Wintle, A.G., and Henshilwood, C.S. 2006b. Extending the chronology of deposits at Blombos Cave, South Africa, back to 140 ka using optical dating of single and multiple grains of quartz. *Journal of Human Evolution* 51(3): 255–273.

Jacobs, Z., Meyer, M.C., Roberts, R.G., Aldeias, V., Dibble, H., and El Hajraoui, M.A. 2011. Single-grain OSL dating at La Grotte des Contrebandiers ('Smugglers' Cave'), Morocco: improved age constraints for the Middle Paleolithic levels. *Journal of Archaeological Science* 38(12): 3631–3643.

Jacobs, Z. and Roberts, R.G. 2007. Advances in optically stimulated luminescence dating of individual grains

of quartz from archaeological deposits. *Evolutinary Anthropology* 16: 210–223.

Jacobs, Z., Roberts, R.G., Galbraith, R.F., Deacon, H.J., Grun, R., Mackay, A., Mitchell, P., Vogelsang, R., and Wadley, L. 2008a. Ages for the Middle Stone Age of southern Africa: implications for human behavior and dispersal. *Science* 322(5902): 733–735.

Jacobs, Z., Wintle, A.G., Duller, G.A.T., Roberts, R.G., and Wadley, L. 2008b. New ages for the post-Howiesons Poort, late and final Middle Stone Age at Sibudu, South Africa. *Journal of Archaeological Science* 35(7): 1790–1807.

Jones, R.L. and Beavers, A.H. 1963. Some mineralogical and chemical properties of plant opal. *Soil Science* 96(6): 375–379.

Katz, O., Cabanes, D., Weiner, S., Maeir, A.M., Boaretto, E., and Shahack-Gross, R. 2010. Rapid phytolith extraction for analysis of phytolith concentrations and assemblages during an excavation: an application at Tell es-Safi/Gath, Israel. *Journal of Archaeological Science* 37(7): 1557–1563.

Kilburn, R. and Rippey, E. 1982. *Sea shells of southern Africa*. Macmillan, Johannesburg.

Lutjeharms, J.R.E. 2006. *The Agulhas Current*. Springer-Verlag, New York.

Madella, M., Alexandre, A., and Ball, T. 2005. International Code for Phytolith Nomenclature 1.0. *Annals of Botany* 96(2): 253–260.

Mercader, J., Runge, F., Vrydaghs, L., Doutrelepont, H., Ewango, C.E.N., and Juan-Tresseras, J. 2000. Phytoliths from archaeological sites in the tropical forest of Ituri, Democratic Republic of Congo. *Quaternary Research* 54(1): 102–112.

Mitchell, P. 1996. Prehistoric exchange and interaction in southeastern southern africa: Marine shells and ostrich eggshell. *African Archaeological Review* 13(1): 35–76.

Namdar, D., Zukerman, A., Maeir, A.M., Katz, J.C., Cabanes, D., Trueman, C., Shahack-Gross, R., and Weiner, S. 2011. The 9th century BCE destruction layer at Tell es-Safi/Gath, Israel: integrating macro- and microarchaeology. *Journal of Archaeological Science* 38(12): 3471–3482.

Olley, J.M., Pietsch, T., and Roberts, R.G. 2004. Optical dating of Holocene sediments from a variety of geomorphic settings using single grains of quartz. *Geomorphology* 60(3–4): 337–358.

Piperno, D.R. 2006. *A comprehensive guide for archaeologists and paleoecologists*. Alta Mira Press, Lanham.

Piperno, D.R. and Becker, P. 1996. Vegetational history of a site in the central Amazon Basin derived from phytolith and charcoal records from natural soils. *Quaternary Research* 45(2): 202–209.

Piperno, D.R. and Pearsall, D.M. 1998. The silica bodies of tropical American grasses: morphology, taxonomy, and implications for grass systematics and fossil phytolith identification. *Smithsonian Contributions to Botany* 85: 1–40.

Porat, N. and Botha, G. 2008. The luminescence chronology of dune development on the Maputaland coastal plain, southeast Africa. *Quaternary Science Reviews* 27(9–10): 1024–1046.

Prescott, J.R. and Hutton, J.T. 1994. Cosmic ray contributions to dose rates for luminescence and ESR dating: large depths and long-term time variations. *Radiation Measurements* 23: 497–500.

Rosen, A.M. and Weiner, S. 1994. Identifying ancient irrigation - a new method using opaline phytoliths from emmer wheat. *Journal of Archaeological Science* 21(1): 125–132.

Rossouw, L. 2009. *The application of fossil grass phytolith analysis in the reconstruction of Cainozoic environments in the South African interior*. University of the Free State.

Runge, F. 1999. The opal phytolith inventory of soils in central Africa - quantities, shapes, classification, and spectra. *Review of Palaeobotany and Palynology* 107(1–2): 23–53.

Sangster, A.G. and Parry, D.W. 1969. Some factors in relation to bulliform cell silicification in grass leaf. *Annals of Botany* 33(130): 315–323.

Shackleton, C.M., Granger, J.E., McEnzie, B., and Mentis, M.T. 1991. Multivariate analysis of coastal grasslands at Mkambati Game Reserve, north-eastern Pondoland, Transkei. *Bothalia* 21: 91–107.

Stromberg, C.A.E., Werdelin, L., Friis, E.M., and Sarac, G. 2007. The spread of grass-dominated habitats in Turkey and surrounding areas during the Cenozoic: Phytolith evidence. *Palaeogeography Palaeoclimatology Palaeoecology* 250(1–4): 18–49.

Taljaard, J.J. 1996. *Atmospheric circulation systems, synoptic climatology and weather phenomena of South Africa*. Part 6, *Rainfall in South Africa*. Government Printer, Pretoria.

Tieszen, L.L., Senyimba, M.M., Imbamba, S.K., and Troughton, J.H. 1979. Distribution of C_3-grass and C_4-grass and carbon isotope discrimination along an altitudinal and moisture gradient in Kenya. *Oecologia* 37(3): 337–350.

Twiss, P.C. 1992. Predicted world distribution of C_3 and C_4 grass phytoliths. In *Phytolith systematics. Emerging issues, advances in archaeological and museum science*, Rapp, Jr., G. and Mulholland, S.C. (eds.). Plenum, New York, pp. 113–128.

Twiss, P.C., Suess, E., and Smith, R.M. 1969. Morphological classification of grass phytoliths. *Soil Science Society of America Proceedings* 33(1): 109–115.

Wintle, A.G. 1997. Luminescence dating: laboratory procedures and protocols. *Radiation Measurements* 27: 769–817.

Yoshida, H., Roberts, R.G., Olley, J.M., Laslett, G.M., and Galbraith, R.F. 2000. Extending the age range of optical dating using single 'supergrains' of quartz. *Radiation Measurements* 32: 439–446.